Title
Magnetic flow cytometry for point-of-care applications

Author
Sridhar, Kaushik

Publication Date
2016

UNIVERSITY OF CALIFORNIA, SAN DIEGO

Magnetic Flow Cytometry for Point-of-care Applications

A Thesis submitted in partial satisfaction of the requirements for

the degree Master of Science

in

Bioengineering

by

Kaushik Sridhar

Committee in charge:

Drew A. Hall, Chair
Pedro Jo Cabrales
Michael J. Heller

2016

The thesis of Kaushik Sridhar is approved, and it is acceptable in quality and form for publication on microfilm and electronically:

Chair

University of California, San Diego

2016

EPIGRAPH

“History repeats, but science reverberates”

― Siddhartha Mukherjee, “*The Emperor of All Maladies*:
A Biography of Cancer”

TABLE OF CONTENTS

LIST OF FIGURES

LIST OF TABLES

ACKNOWLEDGEMENTS

I am grateful to many people who have helped me towards the completion of my Masters' program. First and foremost, I would like to thank my advisor, Dr. Drew A. Hall, whose outstanding vision, intellect and ingenuity have guided me every step of the way. Apart from his scientific guidance, I would forever be indebted to him for encouraging me to think outside the box and inspiring me to continue working in Bioengineering.

Next, I would like to thank Dr. Michael J. Heller, who kindly accepted to be part of my reading committee and introduced me to the field of point-of-care cancer diagnostics through his class. His passion towards the field of nanotechnology is very inspiring and I hope to eventually emulate his never-say-die attitude in research. I would also like to thank Dr. Pedro Cabrales, under whom I had the opportunity to serve as a teaching assistant for two years. Apart from being an inspiring mentor, he is an excellent human being.

I would also like to thank my friends and colleagues, Chih-Cheng (Iric) Huang and Xiahan (Sean) Zhou, for their contribution and for working tirelessly towards the success of this project. Their inputs were crucial in the progress of this project. I thank for their company and for making research immensely enjoyable. I am also very grateful to my co-workers from the Hall Lab for their never-ending support and brain-storming sessions.

I am also very grateful for the company of my dear friends, Bharat Sridhar, Varsha Vijayan, Aishwarya Balakrishnan and Yuchen Wang. They formed a very strong support system in my journey through research and I will be always be beholden to them.

My special thanks goes out to Dr. Utkan Demirci who introduced me to the field of microfluidics and cancer diagnostics. I hope to learn from his ability to integrate multiple fields to bring out pioneering research.

Last but not the least, I would like to thank my parents, Mr. Sridhar and Dr. Gowri, my sister, Sowmya, and my companion for life, Pavithra. Pavithra is the most kind and caring person I have known and am very grateful for her unending love and encouragement. I dedicate this thesis to my family and my extended family.

ABSTRACT OF THE THESIS

Magnetic Flow Cytometry for Point-of-care Applications

by

Kaushik Sridhar

Master of Science in Bioengineering

University of California, San Diego, 2016

Professor Drew A. Hall, Chair

Since the early 1970's, flow cytometry has been an essential biomedical tool for measuring and quantitatively analyzing cells, its applications ranging from hematology to identifying prognostic indicators for cancer, HIV and other time dependent markers of disease activity. Developing countries are at a greater risk of disease, where diagnosis is delayed due to lack of advanced resources. A W.H.O. study reveals that more than 80% of the patients in these countries are already have cancer progressed to advanced stages, at the time of diagnosis. Timely detection of these biomarkers can have a huge impact on the treatment outcome and ultimately the survival rate while simultaneously reducing the economic burden.

Despite the advancements in optical and impedance based flow cytometers for diagnosis, they are limited by a poor readout with high background noise, dependence on cell suspension matrix and photo-bleaching. Magnetoresistance (MR) biosensors overcome all of the above limitations with applications in point-of-care settings. However, prior to developing the MR flow cytometer, it is necessary to model this system based on multiple parameters like the size of the magnetic nanoparticles, applied magnetic force and hydrostatic pressure. As part of this thesis, we optimized the sensing range mathematically and have estimated that a single magnetic bead about 4.5 µm in diameter can be detected by the sensor, while generating a signal as high as 600 mOhms. Microfluidics is incorporated to ensure close contact with the sensor surface with a minimal loss of signal due to diffusion.

Chapter 1 – Introduction

1.1 Motivation

Since the early 1970's, flow cytometry has remained an essential biomedical tool for the measurement and quantitative analysis of cells, ranging from hematology to identifying prognostic indicators for cancer, HIV and other time dependent markers of disease activity. Timely detection of biomarkers for these conditions can have a huge impact on the mortality rate as well as reduce the economic burden. According to Cancer Facts and Figures 2015, it was estimated that more than 1,600 people die every day due to cancer [1-1]. One of the most comprehensive large-scale surveys of medical providers estimated that the direct medical costs for cancer treatment worldwide was a staggering $895 billion. [1-2]. Studies conducted by W.H.O. show that an early detection of cancer greatly increases the chances for successful treatment and can significantly reduce treatment cost as well [1-3]. Hence, there is an urgent need for a sensitive and cost-effective diagnostic platform capable of early detection of cancer to increase survival rates.

Flow cytometry achieves high multiplexing by analyzing single cells flowing through a detection system. Among the various sensing modalities in flow cytometry, optical techniques such as Fluorescent Assisted Cell Sorting (FACS) are considered the gold standard for multi-parameter analysis of complex cell populations. However, since FACS relies on fluorophore or antibody-fluorophore tags for sorting cells, it can suffer from photobleaching [1-4] and autofluorescence [1-5] depending on the laser intensity and fluorophore used and makes it difficult to distinguish cell subpopulations with similar markers. Moreover, increased installation and reagent costs limit the availability of FACS to centralized laboratories. Due to the presence of sophisticated instrumentation, FACS requires highly skilled personnel to operate it and interpret the data. This is particularly debilitating for disease diagnoses in low-resource settings. Though recent advances in multi-color FACS [1-6] enable one to determine multiple cellular characteristics like cell size, cell surface receptors and intracellular markers, its bulky components (light source, flow cell, optical filter units, photomultiplier tubes and data processing unit) complicate point-of-care (POC) instrumentation. Despite a faster processing time and absence of sample pretreatments in impedance-based flow cytometry, the electrical properties of surface molecules, cell size and the matrix produce a noisy environment resulting in a poor readout signal. Conventional diagnostic techniques for cell analysis (cell staining and microscopy) face similar problems along with low-throughput and processing time for sample preparation (tissue processing, fixing and staining) in spite of a high degree of accuracy. While optical flow cytometers are the most widely used mode for analyzing cell populations, the dependence on expensive reagents, the high maintenance costs, and the lack of portability makes it ill-suited for diagnosing patients in developing countries. Hence, there remains a pressing need for a miniaturized, yet sensitive, diagnostic tool that combines the high-throughput offered by flow cytometry with the efficacy of assay-based labeling techniques [1-7].

In this thesis, I lay the foundation and mathematical underpinning for using a magnetoresistance (MR) sensor in a magnetic flow cytometer. Stated simply, the magnetic signature of superparamagnetic particles bound to the target analyte is translated as a change in resistance across the sensor surface. Unlike FACS or impedance flow cytometry, MR-based flow cytometry provides matrix-insensitivity that does not require a constant regulation of pH, temperature, or ionic strength. Concurrently, the absence of magnetic compounds in biological samples reduces the background noise. As this sensor relies on the relative orientation of the different layers, it is possible to obtain real-time monitoring data of the target.

1.2 Organization of the thesis

Chapter 1 highlights the introduction and motivation for this study. Chapter 2 gives an overview of the biosensors used in the point-of-care diagnostics research and the relevant literature review of previous experimental studies. Chapter 3 deals with the description of the materials and protocols used in this research. The mathematical simulations describing expected signal outputs and the integration with a microfluidic platform are covered in chapter 4. The results of hypothesis testing are shown in chapter 5. Discussion, conclusion and future directions are part of chapter 6.

Chapter 2 – Background

2.1 Optical Biosensors – Gold Standard

Advances in microfluidics and nanotechnology has led to tremendous improvements in diagnostics not only in developed nations but also in resource-strapped societies. The reduction in sample volume and high-throughput nature of these platforms have resulted in increased sensitivity. Despite these advances, this method is limited by high cost of consumables and reduced portability of the device.

The primary method of optical detection for flow cytometry applications involves labeling the biomolecules with fluorophores or nanocrystals [2-1]. Upon interaction with the incident radiation (usually laser source), the fluorophores are excited to a higher energy state and emit a longer wavelength before returning to the stable state. It is possible to thus, detect this emitted radiation and enhance it via signal processing techniques. Despite the traditional use of molecular dyes such as Alexafluor 488 (green) or Cy5 (red), improved labelling techniques are available such as quantum dots [2-2].

The typical workflow for such a device involves suspending the target analyte bound with fluorescing bodies in a fluid stream. Usually, a sheath fluid is present to ensure the cells flow in a uniform manner and are concentrated towards the center of the distribution profile. A nozzle is used to control the flow distribution (usually 70 μm). Laser beams positioned orthogonally to the flow are used to excite the labels as shown in Figure 2.1 [2-3]. The resulting emissions of the photons are recognized by a photodetector array to obtain a digital readout. This output can be further processed using specialized transforms [2-4, 2-5, 2-6]. Depending on the number of bound fluorophores, the output signal varies in intensity.

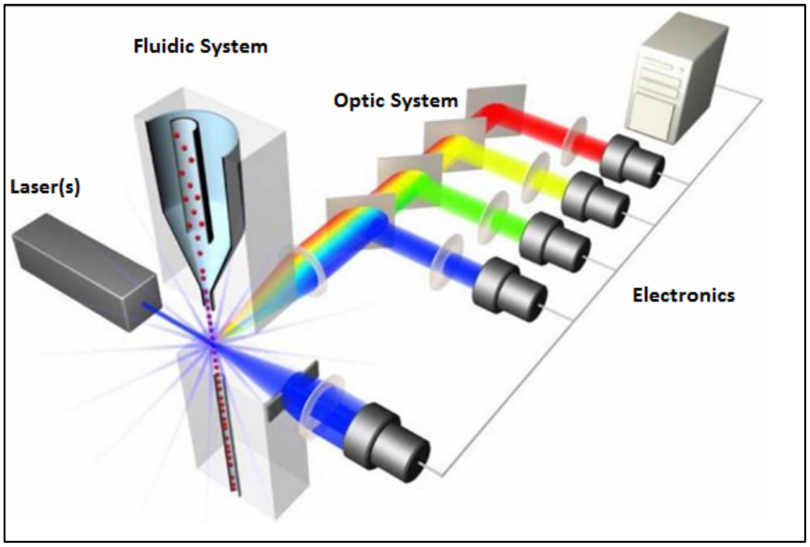

Figure 2.1: Basic components of the flow cytometer

Additionally, these instruments are commonly integrated with cell sorters to differentiate between heterogeneous cell populations [2-7]. Apart from the quantitative and qualitative data obtained by the flow cytometer, a cell sorter aids in collecting discrete cell populations. Usually, a slight vibration is applied to the nozzle creating regular droplets downstream to the excitation radiation. Depending on the diameter of the droplet and the frequency of flow, even single cells can be encapsulated in a droplet [2-8]. Application of an electric charge across the droplet surface will cause it to deflect and hence can be separately collected for further analysis. However, a traditional optical flow cytometer suffers from drawbacks such as high material cost, bulky components, increased possibility of cell contamination, reduced cell viability prior to sorting, and labor intensive [2-9].

It should be noted that there have been significant advances recently to enable the optical flow cytometer for point-of-care applications. The flow cytometry set-up has been miniaturized by combining microfluidics with a cell phone based integrated platform (Figure 2.2), thereby greatly reducing the cost of operation and making it portable [2-10].

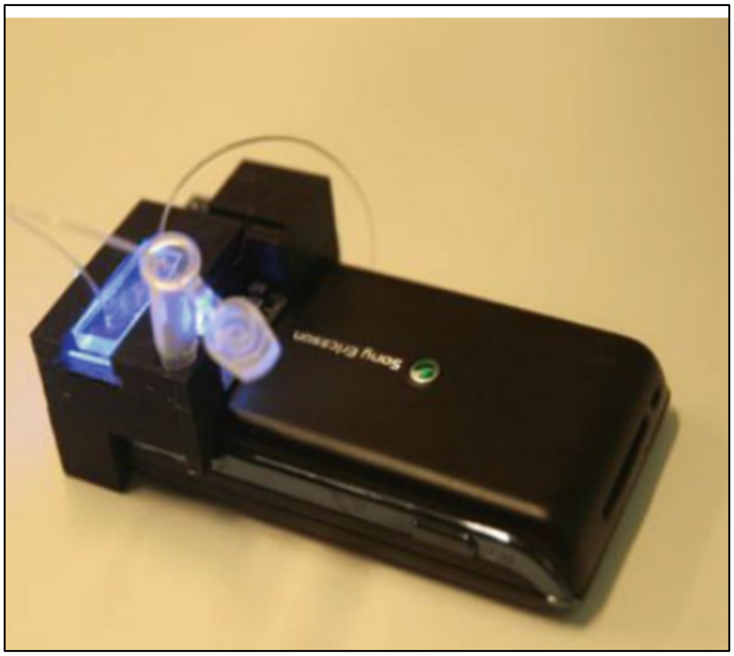

Figure 2.2: Cell phone integrated flow cytometer

A light-emitting diode (LED) is used to provide lateral illumination within a microfluidic chip containing the sample. Similar to the traditional version, the bound fluorophore is excited and the raw images are captured on the complementary metal-oxide semiconductor (CMOS) image sensor of the cell phone. These raw data sets are then digitally processed to reduce the noise and improve the sensitivity via applications on the phone. However, the optical flow cytometers have inherent disadvantages due to photo-bleaching of the bound fluorophores and potential cross-talk between the analytes [2-11].

Another disadvantage with the miniaturized setup of the flow cytometer is the high concentration of fluorophores that are required to generate distinguishable signals [2-12]. It is thus more advantageous to use other modalities as opposed to fluorophore detection to analyze cell of interest.

2.2 Electrochemical Biosensors

Electrochemical biosensors rely on the biochemical signal transduction of analytes or marker compounds resulting in variations in impedance [2-13], current [2-14], conductance [2-15] or capacitance [2-16]. Nowadays, electrochemical biosensors are used in many metabolic measurement assays, the most well-known of these being the glucose biosensor. These class of biosensors offer many advantages over the optical biosensors such as robustness, reduced sensor set-up complexity and can be used with a variety of biofluids irrespective of their optical properties [2-17, 2-18].

Analogous to the optical readouts described in the previous section, electrochemical biosensors commonly use the change in electronic states of redox labels. Based on the oxidative or reductive state of the redox molecule, the biomolecule recognition event is quantified as a function of its concentration. Considering the case of impedance flow cytometry, the prime factor responsible for multi-parametric quantification of the analytes are the dielectric properties of the target cell. Changes in the dielectric properties have been associated with physiological or pathological variations in the cell membrane [2-19]. By integrating this setup with a microfluidic platform it is possible to quantify cellular parameters in a high-throughput manner [2-20]. The cells are allowed to flow through a microfluidic channel incorporated with coplanar microelectrodes to measure the impedance values at multiple frequencies. The multiple frequencies used in these cases provide information related to the concentration, cytoplasmic resistance or the capacitance of the cell membrane (Fig 2.3).

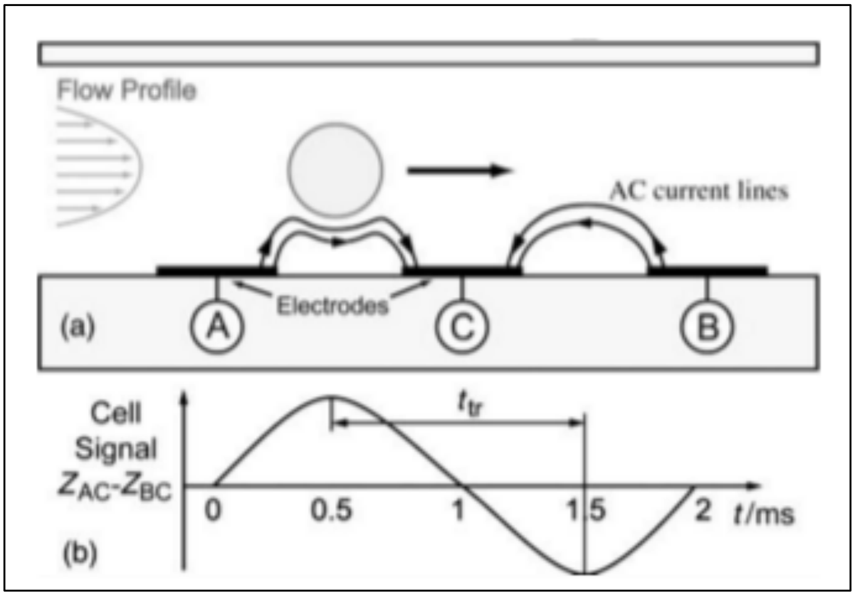

Figure 2.3: a) Flow cell impedance biosensor through microfluidic channels integrated with coplanar microelectrodes b) Measurement of differential impedance values over AC and BC electrodes and velocity of particle (t_{tfr})

In the above figure, the particle is centered using hydrodynamic focusing and hence it is very important that a laminar profile is maintained. Renaud et al. [2-21] were able to derive information about the different cellular components based on the associated frequency spectrum i.e., at low frequencies (40 Hz) the diameter of the cell is obtained due to the obstruction of current flow through the cell membrane while at high frequencies (1 GHz) intracellular components can be studied. Additionally, the velocity of the particle can be estimated based on the time shift in the observed signal and the distance between the electrodes. The signal obtained in this case is highly dependent on the net height of the cell above the electrode surface and it is difficult to control based on hydrodynamic focusing alone.

2.3 Magnetic Biosensors

Using magnetic biosensors overcomes some of the problems associated with optical and electrochemical biosensors namely, matrix sensitivity of the samples contributing to a low signal-to-noise ratio (SNR). Instead of binding the analytes with dyes, they are tagged with magnetic nanoparticles and the stray field produced by them are detected. A wide variety of these tags are commercially available and their diameter ranges from a few nanometers to tens of micrometers [2-22]. The most common techniques used to measure the stray field produced by the magnetic nanoparticles bound to cells are superconducting quantum interference device (SQUID) and magnetoresistive (MR) sensors. Among the MR sensors, Giant Magnetoresistive (GMR) sensors are particularly useful for diagnostic applications due to its high field sensitivity and portability [2-23]. In the following chapters a basic overview of the different magnetic biosensors will be given with a focus on the MR sensors.

2.3.1 Superconducting Quantum Interference Device (SQUID)

SQUID is an extremely sensitive magnetometer that has been used to detect the relaxation in the magnetic moment of MNPs tagged to biological targets [2-24]. It works on a principle known as magnetorelaxation wherein after magnetization by a pulsed magnetic field to align the magnetic moments, the MNPs revert to their original states over a period of time with randomized magnetic moment. They may relax on a faster time scale for unbound MNPs (Brownian Relaxation) or a slower relaxation for bound MNPs (Neel Relaxation). Upon binding the MNPs to known biological targets or pathogens, it is possible to estimate the quantity of bound versus unbound nanoparticles as a function of the relaxation time. However, this device is not very suitable for point-of-care applications as it requires liquid helium at 4.2K to maintain the superconducting state in a magnetically insulated environment [2-25].

2.3.2 Magnetoresistive (MR) sensors

Magnetoresistance is a phenomenon by which a change in an external magnetic field in a material is transduced into a change in resistance. Upon its discovery by Lord Kelvin in 1856, it was observed that the resistance of an iron bar with current flowing through it was decreased when the magnetic field was perpendicular to the current than when it is parallel. The property of a material in which the electric resistance depends on the angle between the direction of the current and the magnetization applied is known as anisotropic magnetoresistance [2-26]. The maximum and minimum resistance observed are related by the magnetoresistance ratio:

$$MR\ Ratio = \frac{R_{max} - R_{min}}{R_{min}} = \frac{\Delta R}{R_{min}}$$

In 1988, the more sensitive GMR sensors were discovered by Albert Fert and Peter Grunberg. GMR spin valve (SV) type sensors which are used in this study, undergo a change in resistance through the quantum mechanical phenomenon of spin dependent scattering. The original applications for GMR sensors include read heads in hard disks [2-27]. The high linearity and low noise of the spin-valve type GMR sensors are extremely useful for the detection of magnetic nanoparticles [2-28, 2-29]. In this regard, one of the most sensitive MR sensors developed is the magnetic tunnel junction (MTJ) sensor. operation is similar to the GMR sensors although it is limited by the large surface area required for biosensing which can be easily fouled by defects [2-30].

The table below compiles the major developments of MR sensors for biosensing.

Table 2.1: Evolution of Magnetic Biosensors and their analytes

Year	Publication	Journal	Analyte	Sensor Type	Citation
1998	Baselt et al	Biosensors and Bioelectronics	DNA	GMR multi layers	2-38
2000	Tondra et al	Journal of Vacuum Science & Technology	MNP	GMR multi layers	2-37
2003	Schotter et al	Biosensors and Bioelectronics	1kb DNA	GMR multi layers	2-39
2005	Shen et al	Applied Physics Letters	MNB	MTJ-Al2O3	2-40
2008	Shen et al	Applied Physics Letters	DNA	MTJ-MgO	2-36
2009	Martins et al	Biosensors and Bioelectronics	20mer DNA	GMR SV	2-35
2010	Hall et al	Biosensors and Bioelectronics	Protein	GMR SV	2-42
2011	Gaster et al	Nature Nanotechnology	Protein	GMR SV	2-34
2012	Lian et al	Journal of Applied Physics	Protein	MTJ-Al2O3	2-33
2014	Fernandes et al	Biosensors and Bioelectronics	Salmonella	GMR SV	2-31
2015	Krishnan et al	Frontiers of Microbiology	Influenza A	GMR SV	2-41

Chapter 3 – Materials & Protocol

The principal cancer diagnostic tool, tissue biopsy, is inconvenient for the patient and relies heavily on skilled technical personnel for a clinical interpretation. The use of GMR SV sensors used in combination with a microfluidic system would avoid the aforementioned problems and will have the potential to process large samples with greater sensitivity compared to conventional procedures [3-1]. In this study, we developed techniques to fabricate a microfluidic channel on top of the GMR SV sensors to restrict the sample to a volume of 20 μL and integrated it with a syringe pump to apply hydrodynamic pressure within the channels.

3.1 GMR SV Sensors

The GMR SV sensors used in this study consist of 16 pins and are fabricated using multi-layer deposition techniques resulting in an eight by eight sensor array with a sensor to sensor pitch of 300 μm (figure 3.1). The sensors used in this platform involved the development of spin-valves on a Si/SiO_2 substrate with thickness (in nm) [3-2]: Ta (3), Seed layer (4), PtMn (15), CoFe(2), Ru (0.85), CoFe (2), Cu (2.3), CoFe (2), Cu (1), Ta (4). A passivation layer of nitrides and oxides of silicon was applied to prevent the corrosive effects of chemical solutions.

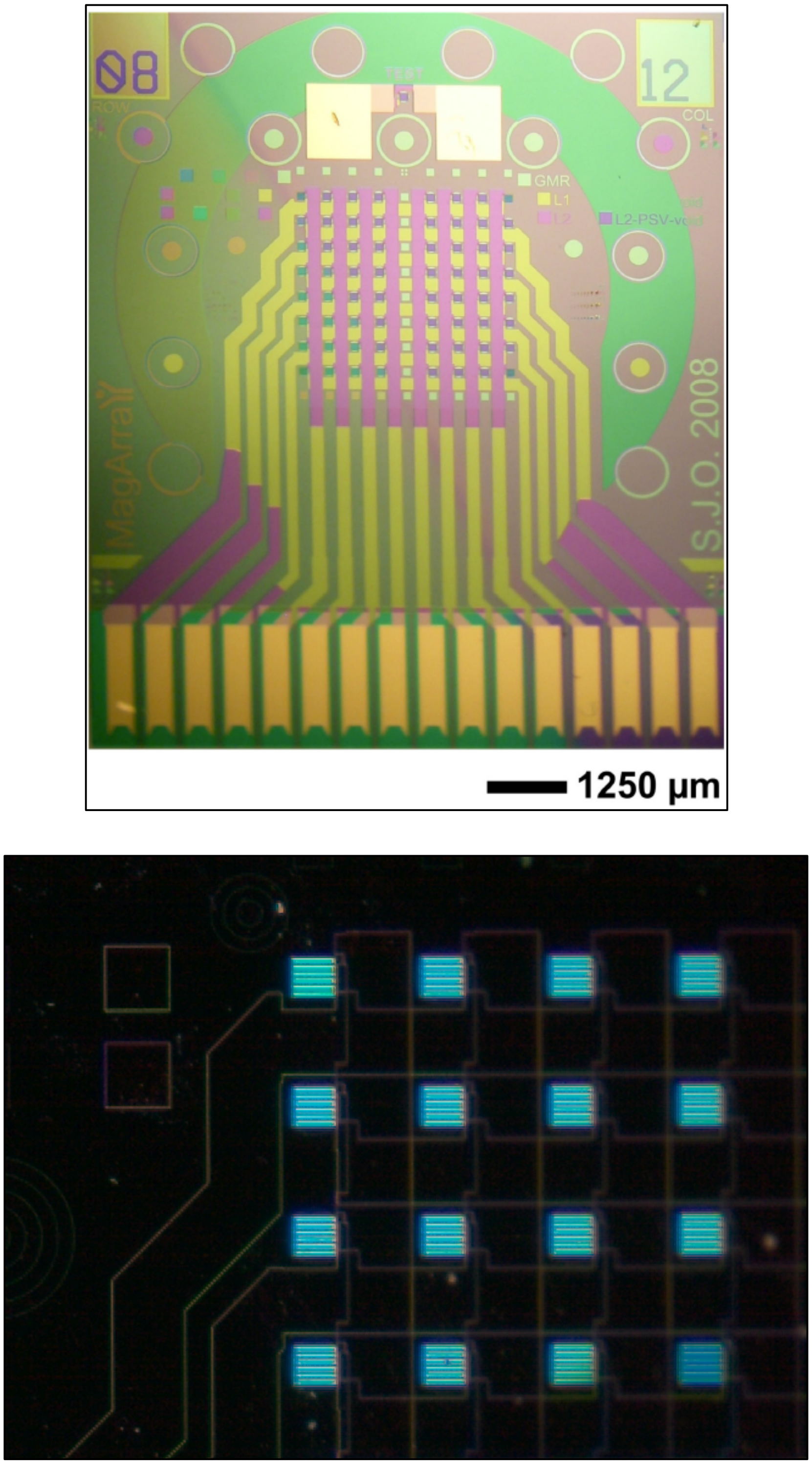

Figure 3.1: GMR SV sensor - orientation of the sensor array.

As illustrated in figure 3.2, the free layer and the pinned layer are ferromagnetic in nature and can hence undergo spontaneous magnetization [3-3].

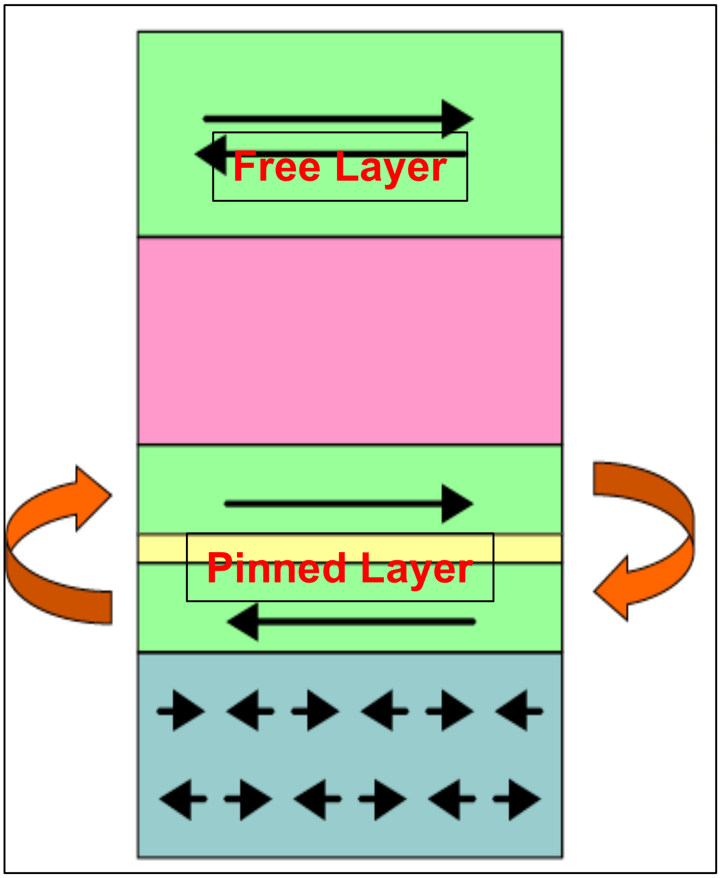

Figure 3.2: GMR SV sensor stacks.

It is thus crucial to create an orderly arrangement of the magnetic domains such that the default orientation of the free layer lies along the linear segment of the anisotropic axis [3-4]. Hence it is highly favorable to have a high aspect ratio to ensure a high reproducibility of the sensor.

3.1.1 MR curve measurements

As the sensitivity of the sensor chip is drastically affected by the presence of any in-plane component of the external magnetic field, its effect was measured by sweeping the sensor surface with an AC sine wave. Additionally, a Helmholtz coil was used to align the magnetic domains in the free layer prior to sample measurements. This experiment would provide the data of the saturation of the sensors due to the in-plane component and prevent loss of sensitivity (figure 3.3).

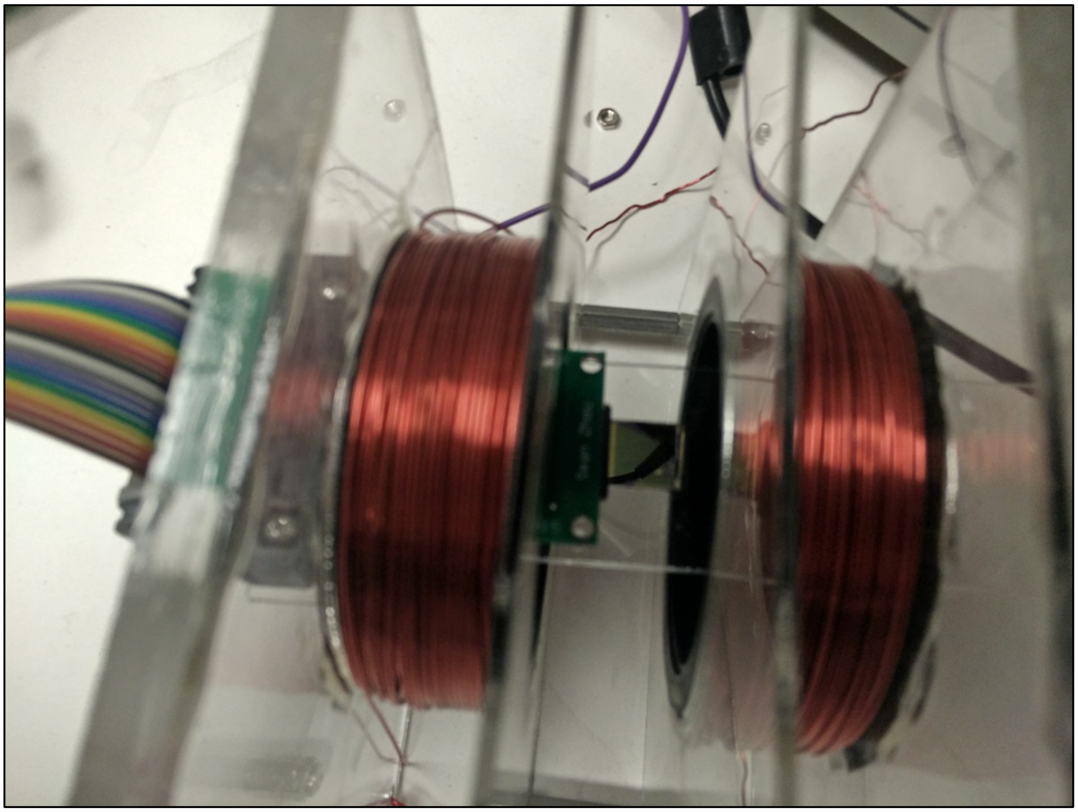

Figure 3.3: Sensor chip in a Helmholtz coil.

The AC sine wave was applied at a frequency of 100 Hz for a duration of 60 seconds. Based on the sweeping magnetic field applied and the change in resistance, the sensitivity of the sensor chip can be determined using the formula:

$$Sensitivity = \frac{dR}{dH} \quad \textbf{(1)}$$

Figure 3.4 denotes the measured changes in resistance over the sweeping magnetic fields using the Helmholtz coil.

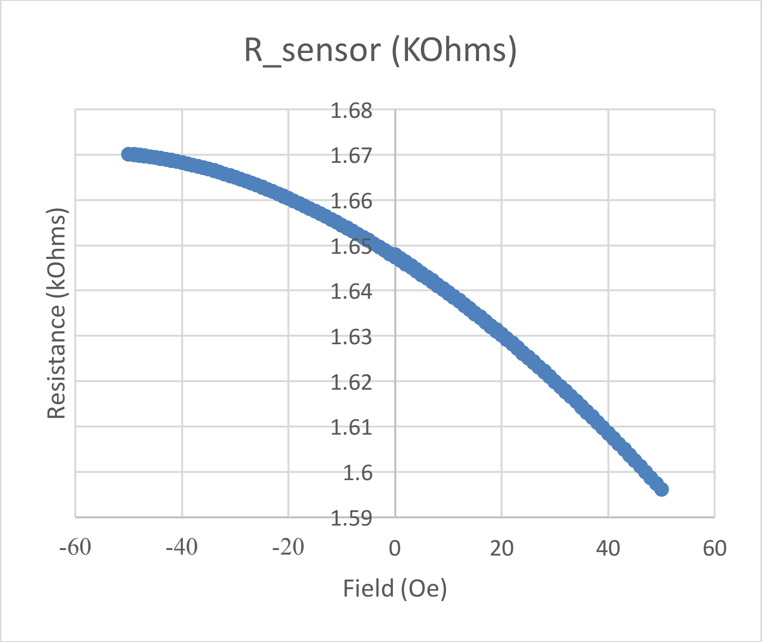

Figure 3.4: Resistance across varying applied magnetic fields

By isolating the linear region of the aforementioned plot, the sensitivity of the chip was found to be 1.03 Ω/Oe (figure 3.4). This data is important in assessing the effects of the tilt of the external magnet and to prevent sensor saturation while choosing the grade of the magnet which can be simulated using finite element models.

3.2 Construction of microfluidic channel

3.2.1 PolyMethylMethAcrylate based channel

An optically clear acrylate double sided adhesive (DSA) having thickness of 25μm was used to fabricate a microfluidic channel having a width of 150-200μm. The fabrication of the channel was done using 100mW CO_2 laser. The laser speed was maintained at 175mm/sec while the power was at 14% of the peak laser output.

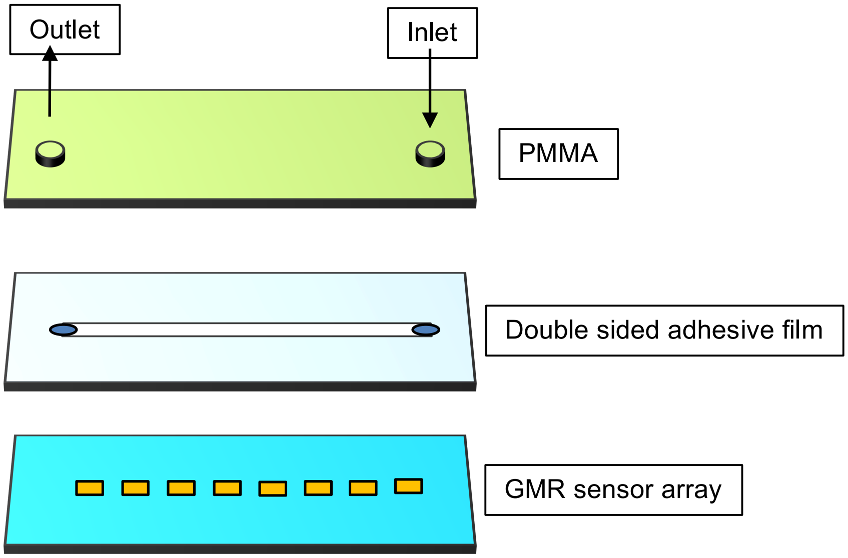

Figure 3.5: PMMA-DSA assembly of microfluidic channel

The inlet and outlet ports of the microfluidic chip was fabricated using the PolyMethylMethAcrylate (PMMA) sheets as the substrate in the laser cutter. The outlines were designed using AutoCAD and were fed into the system such that the final dimensions of the microfluidic chip were 10mm × 5mm. The inlet and outlet ports of the chip was maintained at 0.20 mm to be compatible with Tygon tubing (0.3mm inner diameter) for transporting the sample. As depicted in figure 3.6, the double sided adhesive was aligned along a single column of sensor array (8 sensor blocks).

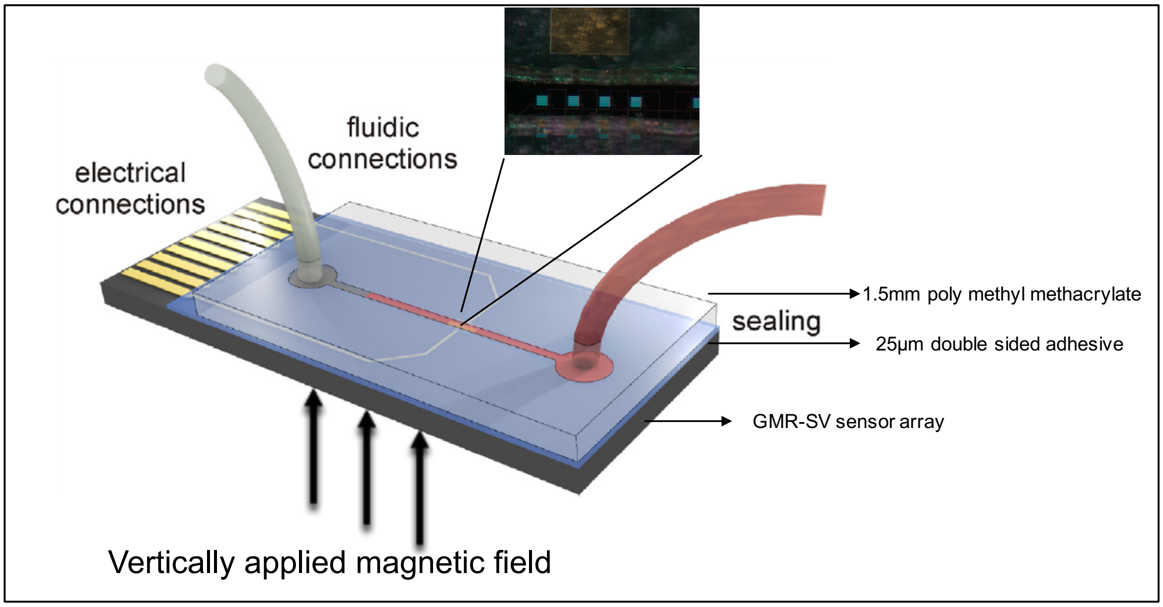

Figure 3.6: PMMA-DSA assembly of microfluidic chip setup

3.2.2 Poly-dimethyl siloxane based channel

Despite the advantages of cost, ease of manufacture and fast turnover time of the PMMA-DSA microfluidic chips [3-5], they are limited by the fabrication via a laser cutter. As the average power of the laser may be too high with respect to the acrylate polymer, most of the times the microfluidic channels are warped due to the heat. This in turn affects the flow regime of the sample through them. As we want to maintain a uniform laminar flow through these channels, the presence of imperfections on the channel walls introduces chaotic mixing and may lead to a reduction in sensitivity. The later chapters will describe the reductions in the sensitivity of the GMR SV sensor as the bead distance increases from the sensor surface. The Poly-dimethyl siloxane (PDMS) microfluidic channel is prepared by the traditional soft lithographic technique [3-6]. Figure 3.7 describes the flow chart for the fabrication of the PDMS microfluidic chip using the SU8-2025 master that was fabricated at the Nano3 Cleanroom at UC San Diego.

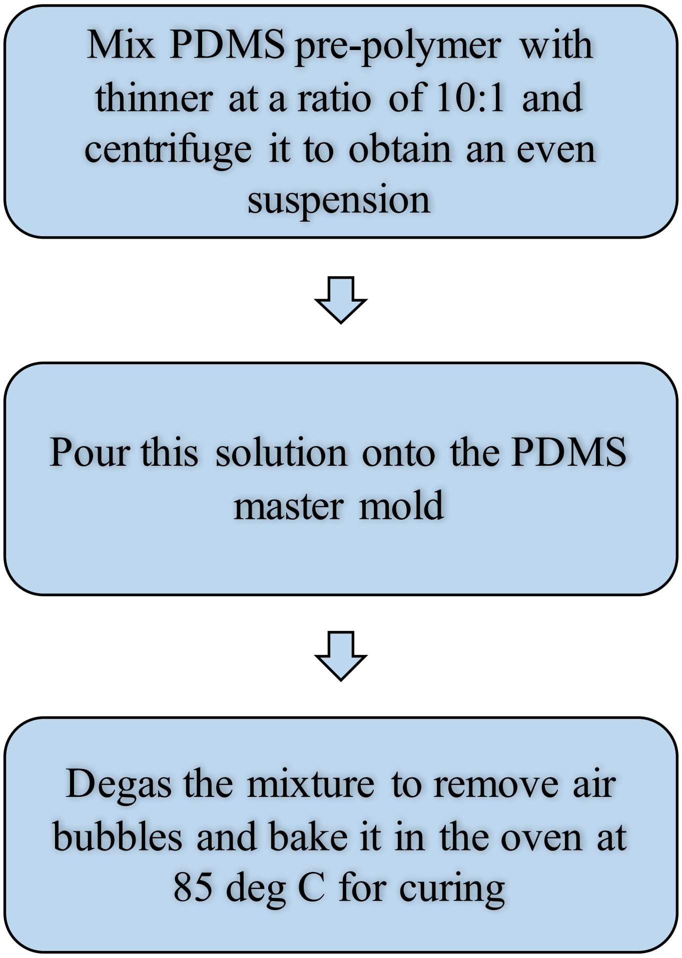

Figure 3.7: PDMS microfluidic chip fabrication

The overall setup was integrated with a syringe pump (Syringe Pump Inc.) to control the volumetric flow rates within the microfluidic channels, figure 3.8. Pressure was applied to create physical bonds in the GMR-SV sensor binding.

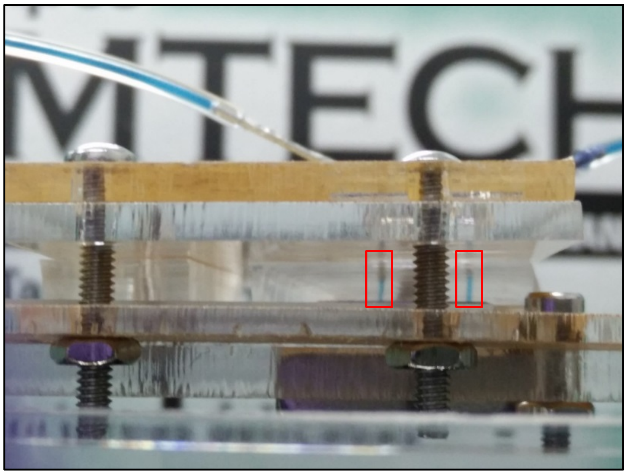

Figure 3.8 PDMS chip assembly with blue dye marking the inlet and outlet.

The maximum burst pressure of this system was calculated to be 750 kPA and can be applied to multiple columns in the future to enable a high-throughput analysis.

Chapter 4 – System Modeling

4.1 Flow Characteristics

The current GMR SV system was designed to be integrated with a microfluidic system to decrease sample processing time and increase sensitivity by restricting diffusion. It is thus important to maintain a uniform flow regime within these microfluidic channel to minimize signal noise generated due to transverse convective mixing. A low Reynold's number was employed to generate a laminar profile due to the presence of extremely small inertial forces that exist within the microstructures [4-1].

COMSOL Multiphysics was used to simulate the laminar flow conditions in a microfluidic channel of width 100 μm and height of 20 μm. Choosing a low Reynold's number (typically < 1000) enables the selection of a laminar flow interface.

Since we are assuming the buffer solution present in the microfluidic channel to have similar physical properties to water, the respective density, dynamic viscosity and the volumetric force of the liquid is chosen under the "Physics" tab of the software. An incompressible Navier-Stokes mode is chosen to model this system. The Navier-Stokes equation is derived from Newton's second law:

$$\boldsymbol{\rho}\left(\frac{d\boldsymbol{u}}{d\boldsymbol{t}} + \boldsymbol{u}.\nabla\boldsymbol{u}\right) = -\nabla\mathbf{p} + \mathbf{F} + \boldsymbol{\mu}(\nabla^2\boldsymbol{u}) \tag{1}$$

where **u** is the fluid's velocity, **F** is the body force exerted on the fluid, **p** is the pressure on the fluid along the length of the channel and μ is the dynamic viscosity of the fluid (Ns/m^2). Three dimensionally this equation can be represented as:

$$\rho\left(\frac{\partial u}{\partial t}+u\frac{\partial u}{\partial x}+v\frac{\partial u}{\partial y}+w\frac{\partial u}{\partial z}\right) = -(\frac{\partial \mathrm{p}}{\partial \mathrm{x}})+\mathbf{F}_x+\ \mu\left(\frac{\partial^2 u}{\partial x^2}+\frac{\partial^2 u}{\partial y^2}+\frac{\partial^2 u}{\partial z^2}\right)\quad (2)$$

$$\rho\left(\frac{\partial v}{\partial t}+u\frac{\partial v}{\partial x}+v\frac{\partial v}{\partial y}+w\frac{\partial v}{\partial z}\right) = -(\frac{\partial \mathrm{p}}{\partial \mathrm{y}})+\mathbf{F}_y+\ \mu\left(\frac{\partial^2 v}{\partial x^2}+\frac{\partial^2 v}{\partial y^2}+\frac{\partial^2 v}{\partial z^2}\right)\quad (3)$$

$$\rho\left(\frac{\partial w}{\partial t}+u\frac{\partial w}{\partial x}+v\frac{\partial w}{\partial y}+w\frac{\partial w}{\partial z}\right) = -(\frac{\partial \mathrm{p}}{\partial \mathrm{y}})+\mathbf{F}_y+\ \mu\left(\frac{\partial^2 w}{\partial x^2}+\frac{\partial^2 w}{\partial y^2}+\frac{\partial^2 w}{\partial z^2}\right)(4)$$

u, v and *w* denote the x, y and z components of the fluid velocity.

Since under low Reynolds number conditions, the inertial forces are minimal, they can be neglected to give:

$$\rho\left(\frac{du}{dt}\right) = -\nabla \mathbf{p}+\mathbf{F}+\ \mu(\nabla^2 u)\quad (5)$$

A "No Slip" boundary condition is set for the walls of the channel. This models the fluid layer closest to the wall to have zero velocity. Since the dimensions of the microfluidic channel are small, under a low flow rate this would be a reasonable assumption to make.

A low volumetric flow rate of 3 $\mu L/min$ was chosen to model here to visualize the location of the peak velocity. In a rectangular cross section of height H, length L and width W, the pressure drop between the two ends of the channel is represented as [4-2]:

$$\Delta P = \frac{a\mu Q L}{W H^3}\quad (6)$$

and **a** is defined by:

$$\mathrm{a} = 12\left[1-\frac{192\mathrm{H}}{\pi^5 W}tanh\left(\frac{\pi W}{2H}\right)\right]^{-1}(7)$$

The velocity field of the laminar flow in a microfluidic channel of L = 1mm, W = 100μm and H = 20μm is simulated in COMSOL:

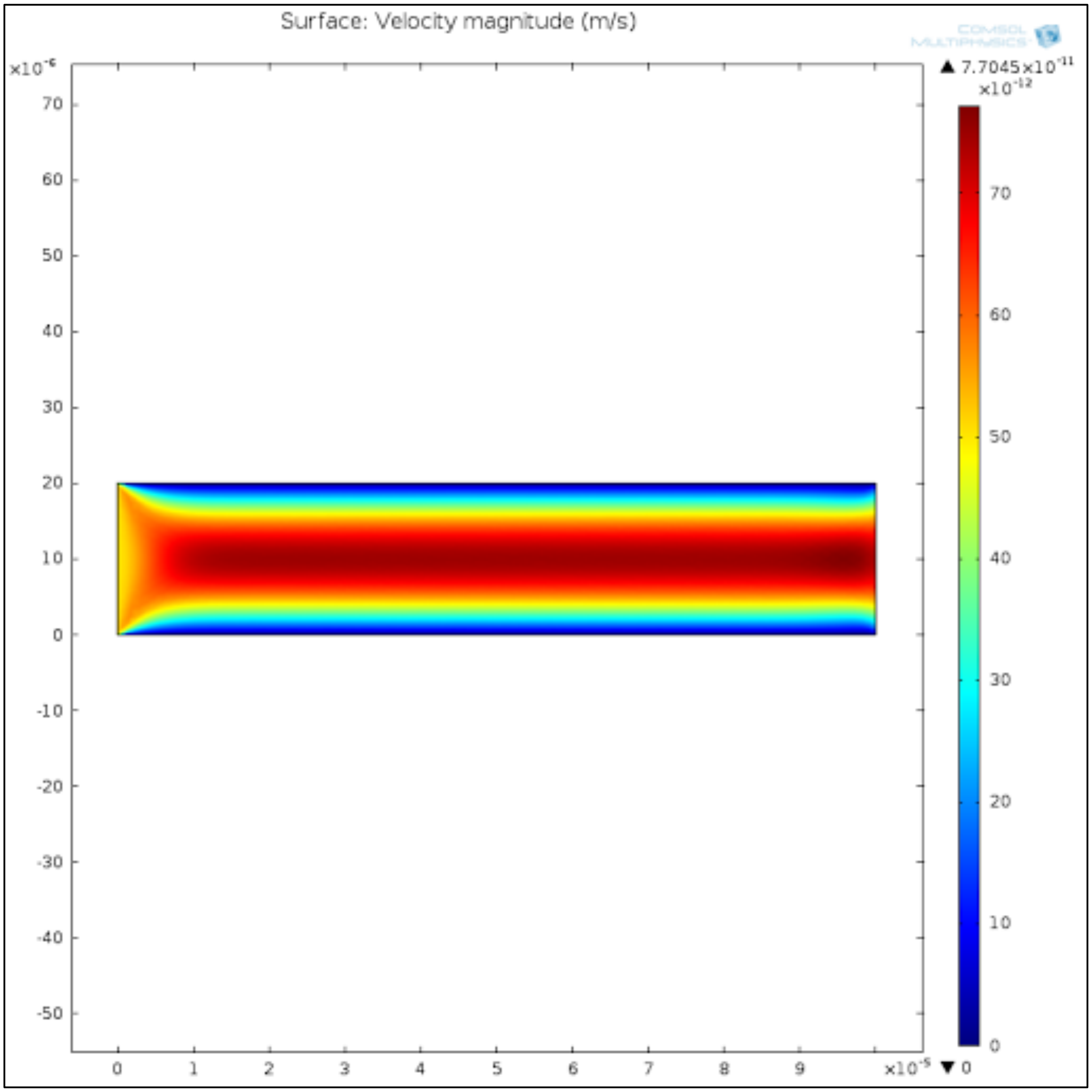

Figure 4.1.1: Velocity profile in a laminar regime

A peak velocity of approximately $70 \times 10^{-12}\ m/sec$ was achieved towards the middle of the channel at 10 μm. In the color gradient, red indicates peak velocity while blue indicates the lowest velocity (zero).

The velocity profile can be extracted as a function of distance from the walls of the microchannel to evaluate the velocity at a distance 'd'.

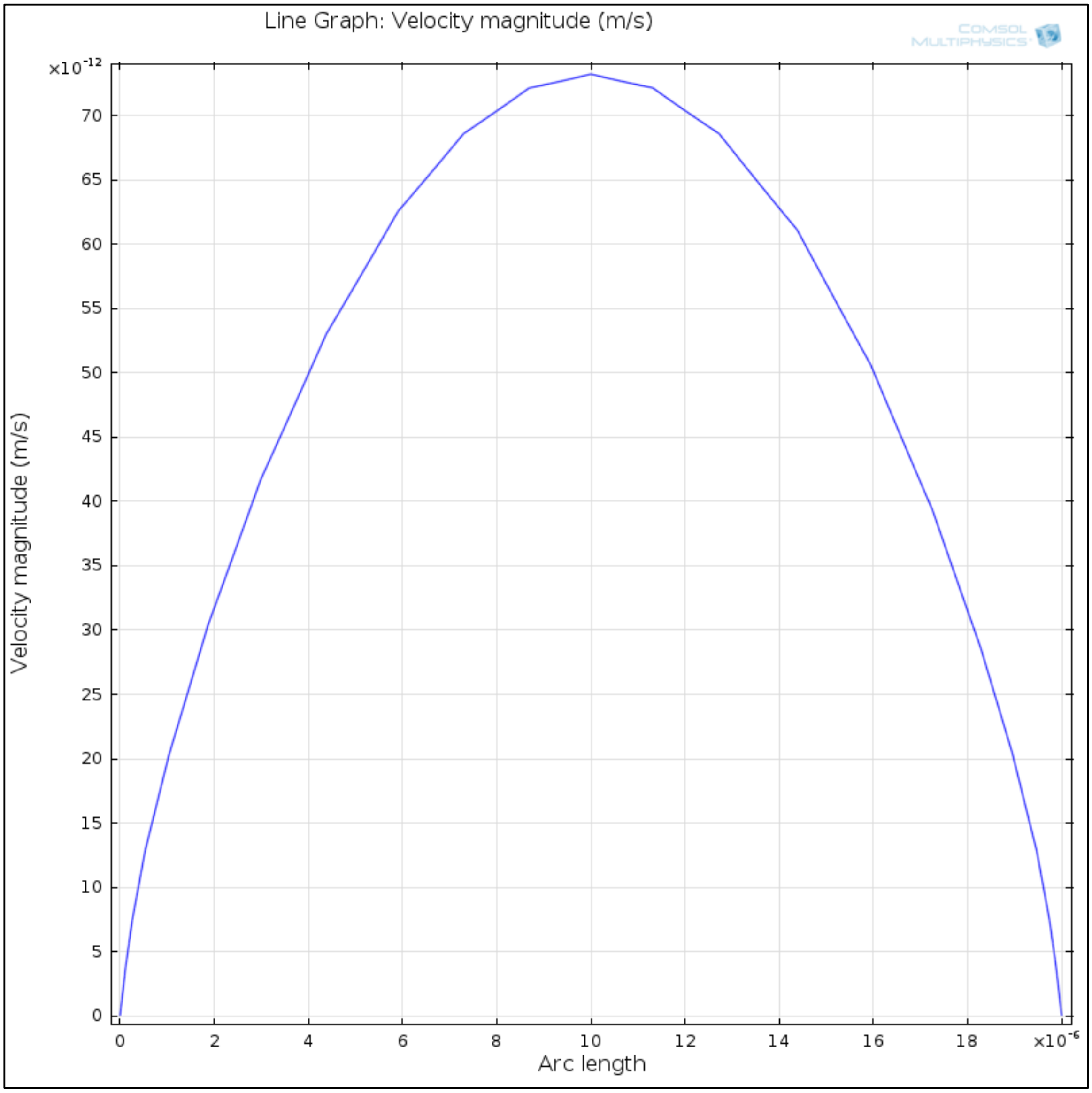

Figure 4.1.2: Velocity profile as a function of distance from the walls of the channel.

4.2 MR simulation for FCM chips

As described in chapter 3, each sensor block within the GMR SV chip is 108 μm long and consists of 6×8 sensor strip lines. The change in resistance over these sensor strips is measured as the magnetic nanoparticles (MNPs) flow over the surface by the application of hydrodynamic pressure.

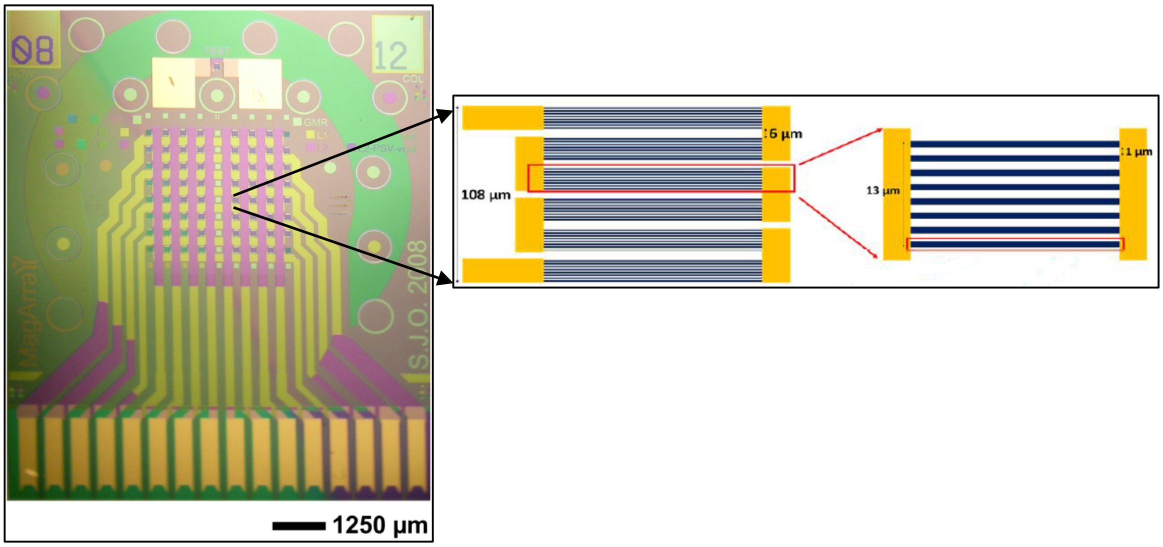

Figure 4.2.1: GMR SV chip geometry and dimensions of sensors

Since the goal of this project is to detect biological analytes tagged with magnetic nanoparticles, beads of different diameters and magnetic susceptibilities are modelled here [Table 4.2]. The signal change in $m\Omega$, is estimated along the short as well as the long axis of the sensor strip (Figure 4.2.1). Additionally, as each of the sensor strips are arranged in a parallel combination, the net signal is also estimated for this case.

Table 4.2: Magnetic bead parameters

Bead	Radius (µm)	Susceptibility
Dynabead M450	2.25	1.632
Dynabead M280	1.415	1.377
Dynabead MyOne	0.5	0.756

4.2.1 Resistance change over the sensor surface

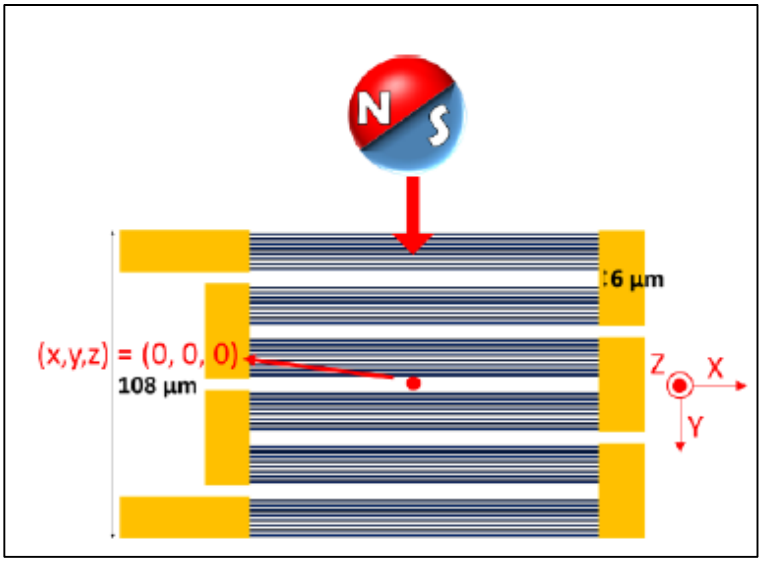

Figure 4.2.2: Sensor block dimensions and direction of bead flow

The magnetic field detected by the sensor is described by the equation [4-3]:

$$< \boldsymbol{H_{y'sensor}} > = \left(\frac{\chi H_z R^3}{lwt}\right) \int_{z=-\frac{t}{2}}^{z=\frac{t}{2}} \int_{y=-\frac{w}{2}}^{y=\frac{w}{2}} \int_{x=-\frac{l}{2}}^{x=\frac{l}{2}} \frac{H_z(z-z_0)(y-y_0)}{r^5} \boldsymbol{dxdydz} \qquad \textbf{(1)}$$

where $< H_{y,sensor} >$ is the spatially averaged magnetic field on the sensor along the short axis ($\vec{y}$) from the beads being magnetized by an external field $\overrightarrow{H_{ext}}$. The field component along the long axis ($\vec{x}$) of the sensor strip can be ignored as we assume that the free layer anisotropy is stabilized by the application of the external magnetic field. Hence, in this derivation it is sufficient to consider the short axis of the sensor strip. 'l' is the length of each strip ($100\mu m$), 'w' is the width ($0.75\mu m$) and 't' is the thickness of the strip (1.5 nm). $\vec{r}$ is the position vector defined by $(x - x_0, y - y_0, z - z_0)$. Additionally, it is assumed that the external field from the permanent magnet is predominantly in the z direction and the in-field components of the permanent magnets are neglected. As M-450 beads have the highest magnetic susceptibility we used these beads for our initial simulations. The distance between the bead and the sensor surface is illustrated in figure 4.2.3.

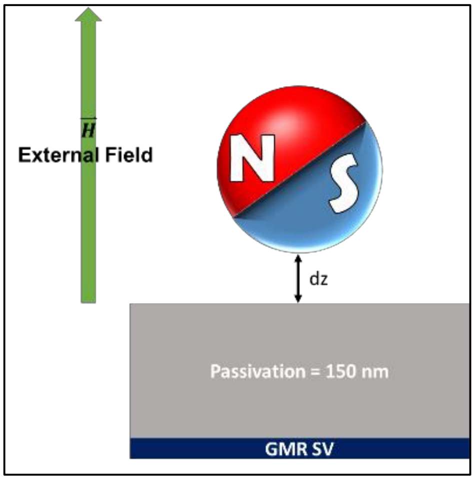

Figure 4.2.3: Orientation of magnetic bead over the sensor

Resistance change can thus be simulated for different magnetic beads and as a function of distance from the surface of the sensor [Figure 4.2.4]. The parameters considered in this simulation are described in Table 4.3.

Table 4.3: Sensor parameters

<table>
<tr><td>Bead</td><td colspan="2">Radius (μm)</td><td>Susceptibility</td></tr>
<tr><td>Dynabeads M-450</td><td colspan="2">2.25</td><td>1.632</td></tr>
<tr><td colspan="2">Sensor Dimension</td><td colspan="2">$100\mu m \times 750$ nm × 1.5 nm</td></tr>
<tr><td colspan="2">R_0 $(Resistance\ in\ ohms)$</td><td colspan="2">2400</td></tr>
<tr><td colspan="2">Sensitivity (S_0 $in\ \Omega/Oe$)</td><td colspan="2">0.6833</td></tr>
</table>

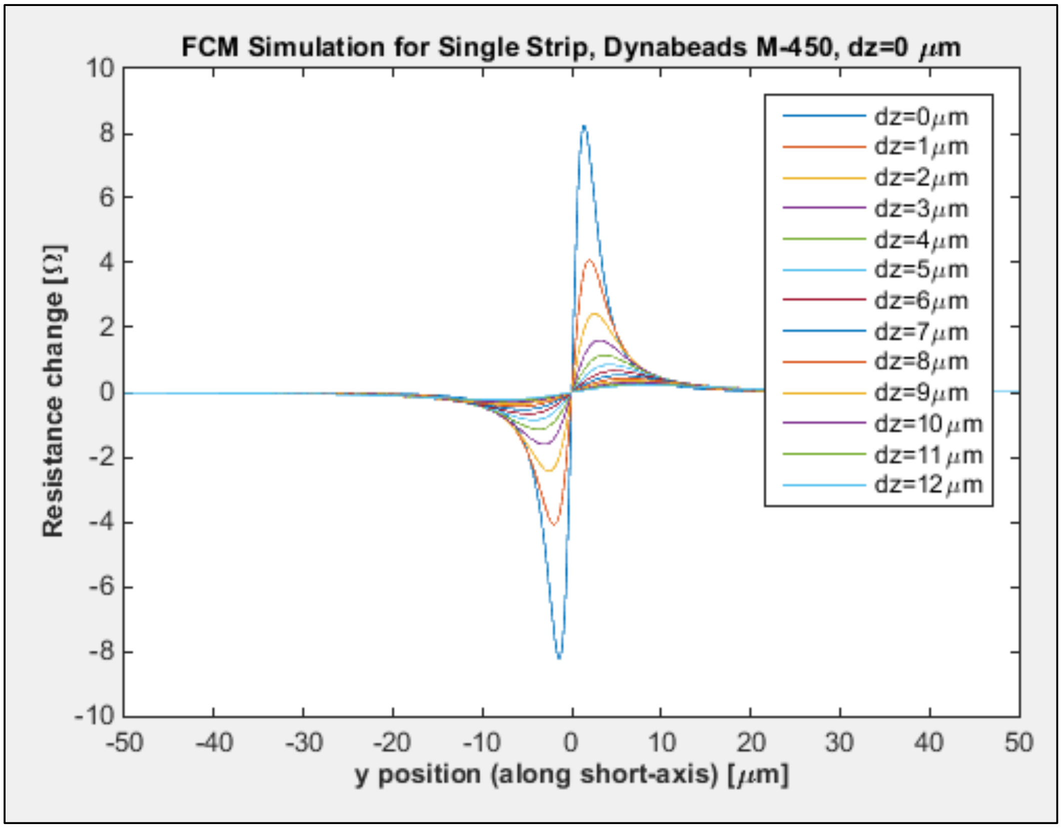

Figure 4.2.4: Resistance drop in single sensor strip

The bimodal peak observed in this simulation occurs due to the orientation of the stray fields as the bead passes over the sensor surface.

Similarly, the simulations were repeated to look at the signal change along the long and short axis for M-450 over 1, 13 and 78 strips respectively, in different chip configurations. (Figure 4.2.5).

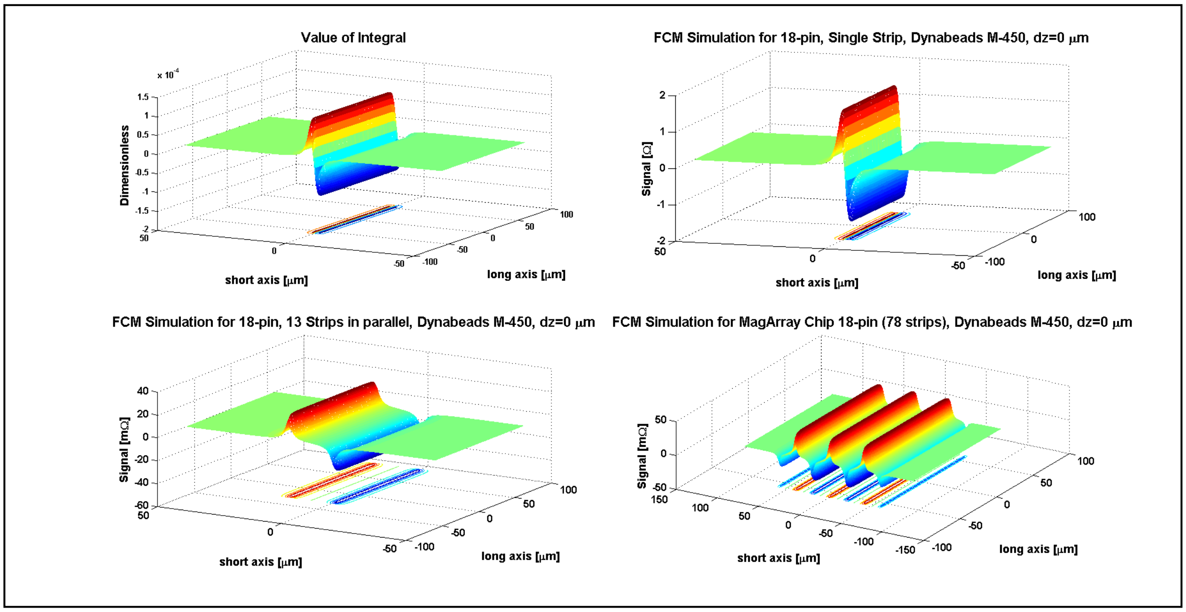

Figure 4.2.5: Resistance changes due to M-450 stray fields.

Since the short axis would be primarily used for our sensing platform, the signal change in $m\Omega$ is plotted for the short and long axis above the sensor surface (figure 4.2.6).

Based on the direction of the stray field, the free layer is either in a parallel or antiparallel orientation [4-3].

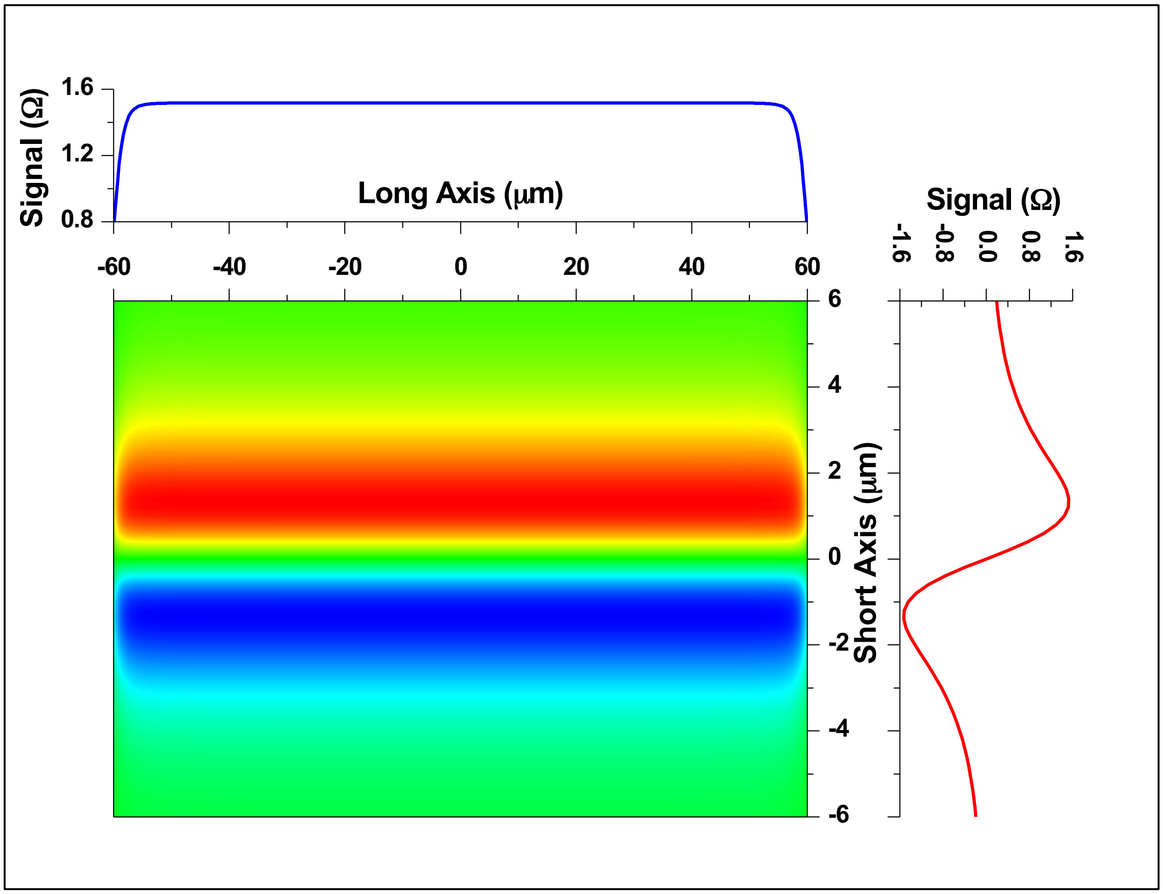

Figure 4.2.6: Resistance change along the axes over single sensor strip due to M-450 stray fields along the long and the short axis.

4.2.2 Resistance change over distance

Using the formula described in the previous section, the resistance change was plotted as a function of bead type (MyOne, dynabeads M-280 and M-450) and distance above the sensor surface. The same parameters as described in Table 4.3 is used here. The sensitivity of the sensor strips are described as follows:

$$\mathbf{Sensitivity} = \frac{\mathbf{dR}}{\mathbf{dH}} \ \mathbf{(8)}$$

Resistance change was thus compared using a single strip line over the different bead types, figure 4.2.7.

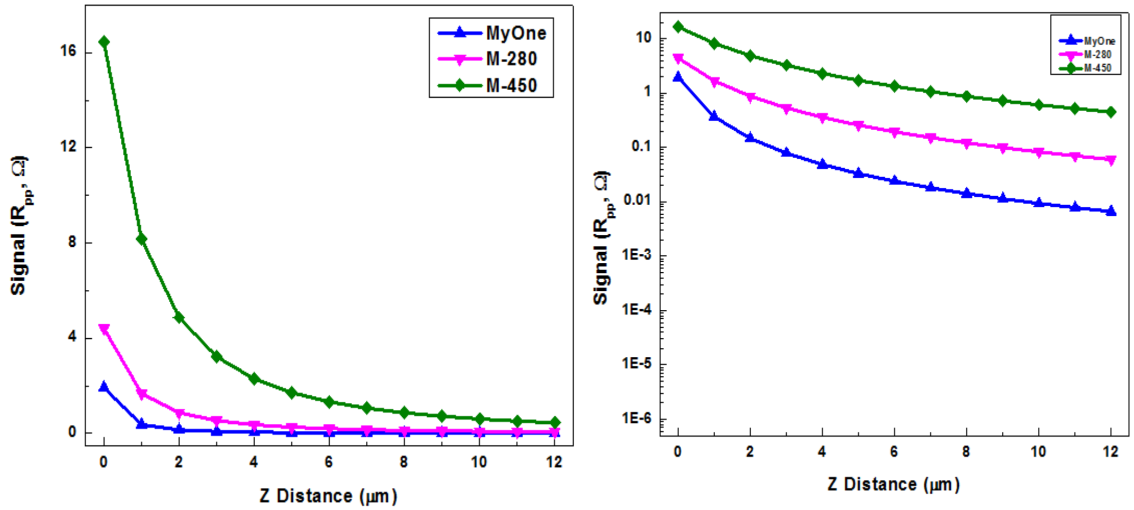

Figure 4.2.7: Resistance change over distances left -Resistance change comparison for single strip line, Right – Logarithmic resistance change.

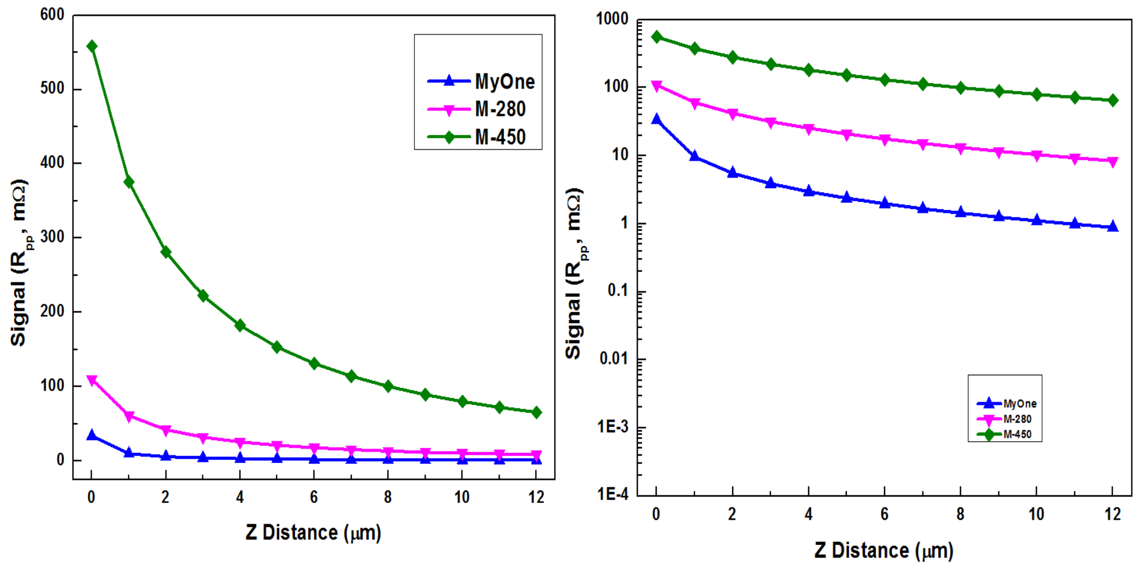

Figure 4.2.8: Resistance changes over sensor block left - resistance change comparison for 48strips over different distances from sensor surface, Right – Logarithmic resistance change.

According to figure 4.2.8, it is observed that the signal reduces approximately at $1/z^3$ where 'z' is the distance above the sensor surface.

4.2.3 Effect of magnetic force on magnetic beads

It is important to quantify the magnetic force experienced by the beads to analyze the particle motion above the sensor surface. Based on the volume fraction of the bead and the magnetic field gradient, the force on the bead can be calculated in the x and y direction.

$$F_{mag,x} = V_b f(B)/\mu_o \left[B_x(x,y)\frac{\partial B_x(x,y)}{\partial x} + B_y(x,y)\frac{\partial B_x(x,y)}{\partial y}\right]$$

$$F_{mag,y} = V_b f(B)/\mu_o \left[B_x(x,y)\frac{\partial B_y(x,y)}{\partial x} + B_y(x,y)\frac{\partial B_y(x,y)}{\partial y}\right]$$

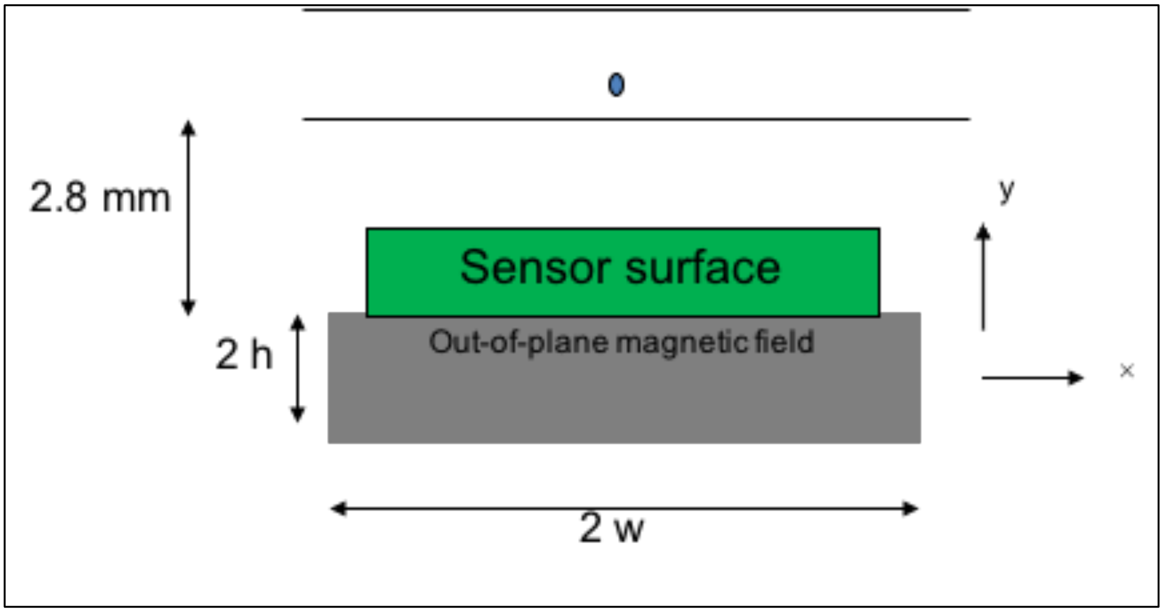

Figure 4.2.9: Illustration of sensor-bead positioning

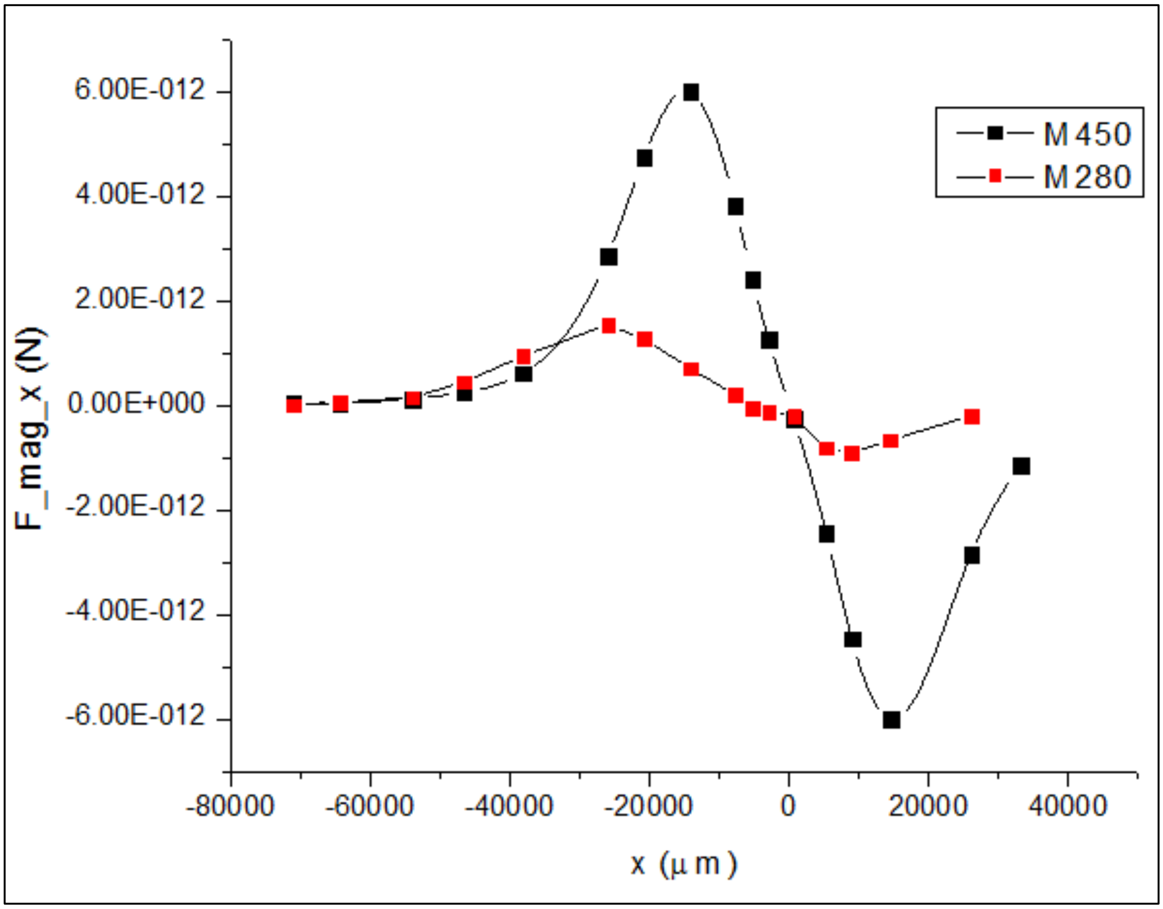

Figure 4.2.10: MATLAB simulation of magnetic force on bead

Based on the magnetic force differential equations described, the peak magnetic force in the x axis for M450 beads was calculated to be 6pN and that if M 280 beads was approximately 2 pN.

Chapter 5 – Results

In this chapter, we give an overview of the in-plane measurements of the external magnetic field, results for the deposition of magnetic beads on the sensor system and a flow based measurements of the magnetic beads in the microfluidic platform.

5.1 In-plane component measurement in GMR chip

As described in chapter 4, the in-plane component of the external magnetic field has to be measured to evaluate whether the sensor is being saturated. In case it saturates the sensor, either the grade of the magnet used would have to be reduced or the distance between the magnet and the sensor surface would have to be increased. Using the Helmholtz coil mentioned in chapter 4, the resistance measurements were repeated in the presence and absence of an external magnetic field. Since the sensitivity of the chip was calculated to be 1.03 Ω/Oe, the values can be substituted in equation (1):

$$Sensitivity = \frac{dR}{dH} \tag{1}$$

Accounting for the temperature drift, the processed resistance in a single sensor column of the chip is obtained in figure 5.1.

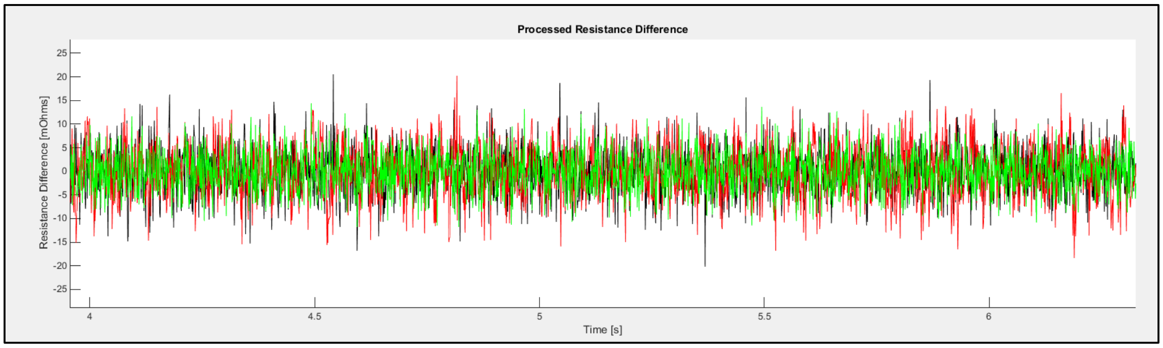

Figure 5.1: Processed resistance in sensor column

In the presence of an external magnetic field, the average resistance measurements from the GMR-SV sensor chip was found to be 1.6758 kOhms. Similar measurements were obtained in the absence of an external magnetic field yielding a value of 1.6945 kOhms.

By plotting the resulting resistance change as a function of the magnetic field, we obtain the in-plane component of the external magnetic field, figure 5.2.

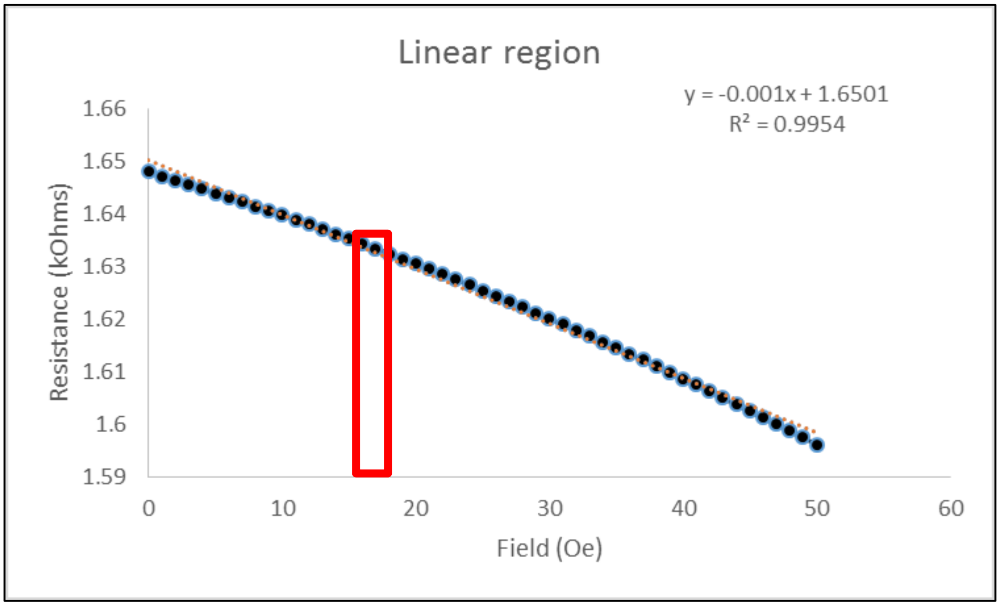

Figure 5. 2: Change in resistance as a function of *dH*

Using the above plot we observe that the in-plane component which is calculated as 18.15 Oe lies in the linear region of the dR/dH curve and hence is not saturated. Thus, the batch of chips used in this study can be used for the sensing purposes given the current microfluidic platform.

5.2 Resistance change with dried beads

Prior to integrating the sensor with the PDMS microfluidic channel, sensor measurement was done by adding $5\mu L$ of the dynabeads M-450 to the sensor rows and measurement was done to note the change in resistance. Though the sensitivity of the sensor would be affected as the bead solution dries on the sensor surface, we were able to notice the regions of the sensor chip from row 1 column 1 (R1C1) to row 5 column 5 (R5C5) which correspond to the droplet location. As shown in figure 5.3, the black boundary denotes the location of the droplet in a sensor array consisting of 64 elements (8 × 8).

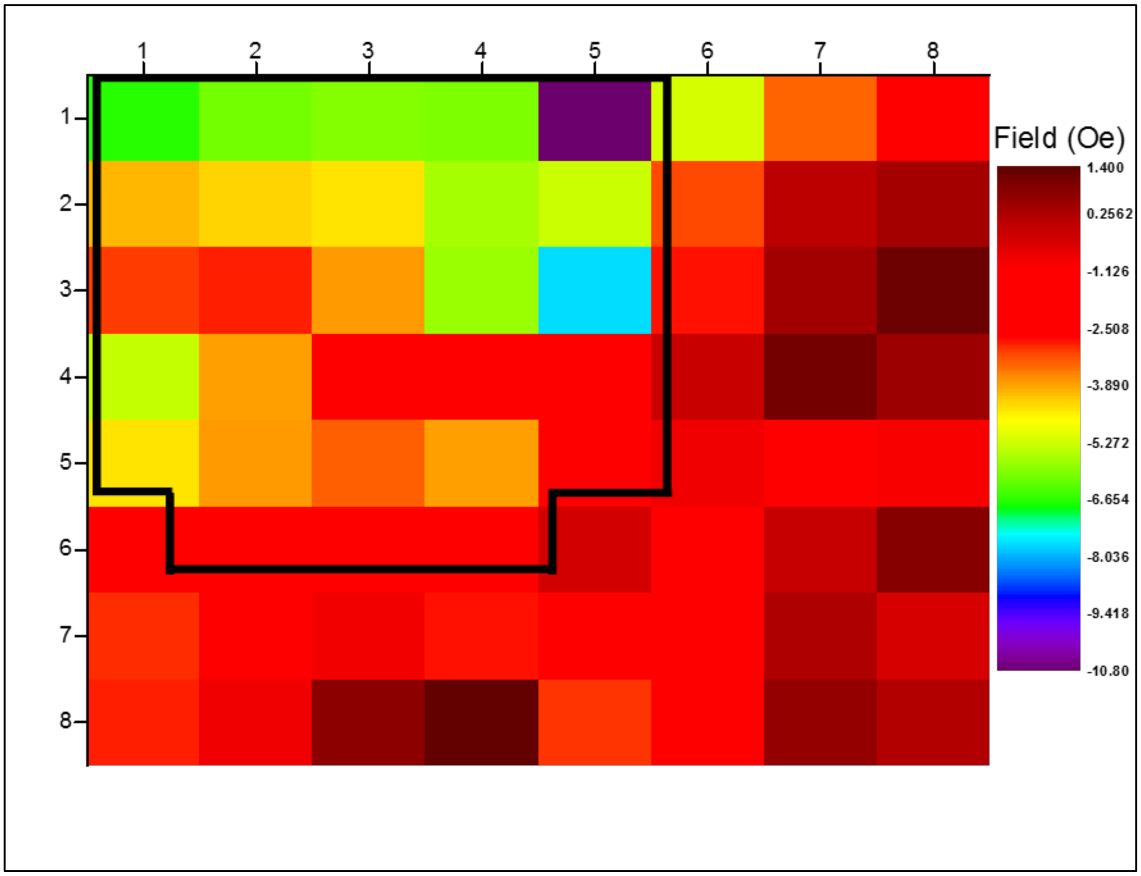

Figure 5.3: Resistance change due to magnetic bead droplet

The change in resistance due to the stray magnetic fields from the magnetic beads M-450 were calculated as 1.532 Ω. Though it should be noted that due to the eventual drying of the beads, they tend to physically cluster and will eventually damage the sensor surface.

5.3 GMR-SV platform to detect magnetic beads

The PDMS based microfluidic system was integrated with the GMR-SV sensor. The microfluidic channel was aligned over a column of sensor blocks and was sealed using pressure applied by the PMMA module on top of the PDMS channel as shown in figure 5.4. The system was carefully calibrated so as to prevent the channel from collapsing while maintaining a tight seal to prevent leakage. The entire platform was also linked with a syringe pump to maintain a constant flow rate for the movement of the solution.

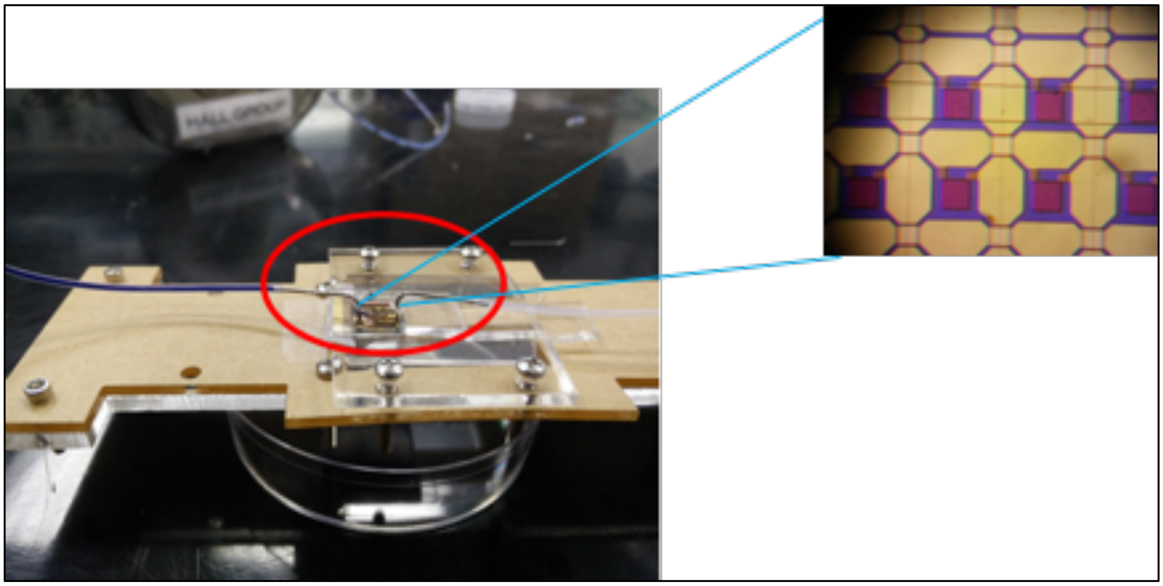

Figure 5.4: Microfluidic assembly with GMR-SV sensor chip

As described in the simulations of the flow rate, a constant laminar flow was applied to enable the movement of the M-450 particles. Despite the super paramagnetic nature of these beads they tend to aggregate in clusters due to the presence of attractive magnetic forces [5-1]. Hence, a high flow rate of 90 $\mu L/min$ was chosen to prevent the formation of these clusters and allow the motion of single beads over the sensor surface. The sensors from different rows named sequentially, Row 1- Row 8, was labelled using the colors described in Table 5.1.

Table 5.1: Color label for the eight sequential sensors

Row 1	Navy
Row 2	Black
Row 3	Red
Row 4	Green
Row 5	Purple
Row 6	Cyan
Row 7	Brown
Row 8	Orange

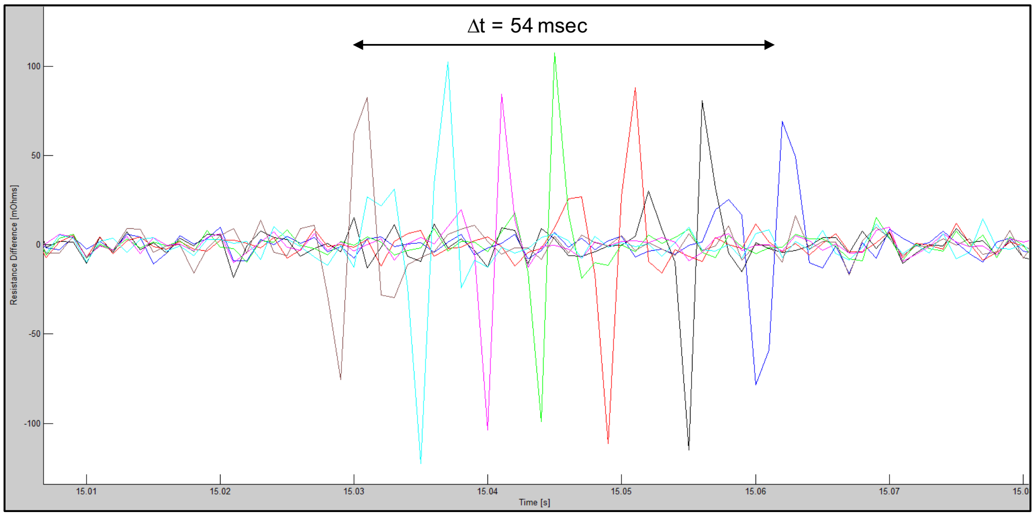

Figure 5.5: Sequential signal response from 8 sensors

As shown in figure 5.5, the bead velocity can be calculated from the time interval between two peaks of signal from the adjacent sensors. From the MATLAB program written by Xiahan Zhou from our lab, average peak to peak resistance (R_{p-p}) was found to be 230 $m\Omega$. The bead velocity was thus estimated to be 6.77 cm/sec. Additionally, based on the amplitude of the individual peaks, the maximum and minimum velocity of the beads were estimated to be 8.125 cm/sec and 5.416 cm/sec respectively.

Thus, given the simulations of the signal response as well as the preliminary data with super paramagnetic beads, it will be possible to detect target cell of interest using a portable, microfluidic GMR-SV platform capable sensitive analyte detection.

Chapter 6 – Discussion

In this chapter, I wish to give an overview of the challenges, future directions and potential impact of this research.

6.1 Sources of error

As described in Chapter 4, the sensitivity of the sensor is inversely proportional to the applied tickling field and thus any tilt in the magnet would contribute to a decrease in the sensitivity of the sensor [6-1]. Apart from the thermal noise in conductors, GMR-SV sensors also exhibit Barkhausen noise which occurs due to the generation and destruction of the magnetic domains during the magnetization reversal of the sensing layer [6-2]. This causes discrete resistance changes which may occur in the absence of the MNPs resulting in faulty signal detection as shown fig. 6.1.

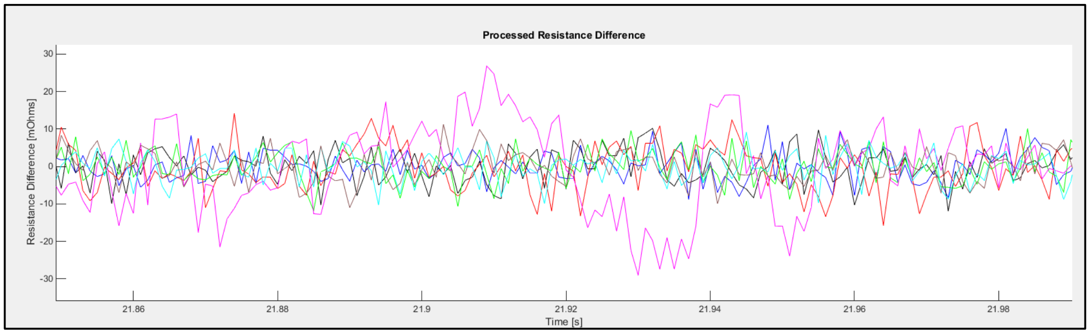

Figure 6.1: Background noise signal of 15-30 mΩ in the absence of sample

However, this can be rectified by applying a strong pre-magnetizing field to order the internal magnetic domains prior to running the sample. Another possible source of error is from the sample itself, wherein the MNPs can form clusters either due to a damaged iron shell or the presence of surface charges resulting in an inaccurate detection [6-3].

The consistency of the GMR-SV sensors should be tested repeatedly as they might be subject to fouling based on the handling of the sensors.

6.2 Future directions

Currently, the studies describe the theoretical parameters and the design for the microfluidic integration to GMR-SV sensors. Future studies are planned to evaluate the sensitivity of these sensors in the detection of circulating tumor cells from human blood. We also intend to demonstrate the selectivity and sensitivity of this system to other MNP based bioassays for diagnostic as well as therapeutic purposes including drug efficacy studies. The model will also be refined using finite element analysis to ensure appropriate meshing parameters are incorporated to evaluate the velocity of the analyte bound with MNPs.

6.3 Potential Impact

Conventional diagnostic techniques are time consuming and require centralized laboratories for handling sample preparation and analysis [6-4]. Therefore, it is necessary to have rapid and sensitive platforms that can process large volumes and a high degree of matrix stability during analysis. Conditions like cancer metastasis, which is the leading cause of cancer related deaths [6-5], can be detected early by the quantification of circulating tumor cell based prognostic indicators. Patients can be spared from unnecessary needle based biopsy which can cause discomfort as well as lead to secondary infections. The development of a microfluidic GMR-SV biosensor platform would thus eliminate the abovementioned effects and enhance the quality of patient care as well as provide clinicians with an accurate and portable diagnostic device as shown in figure 6.2.

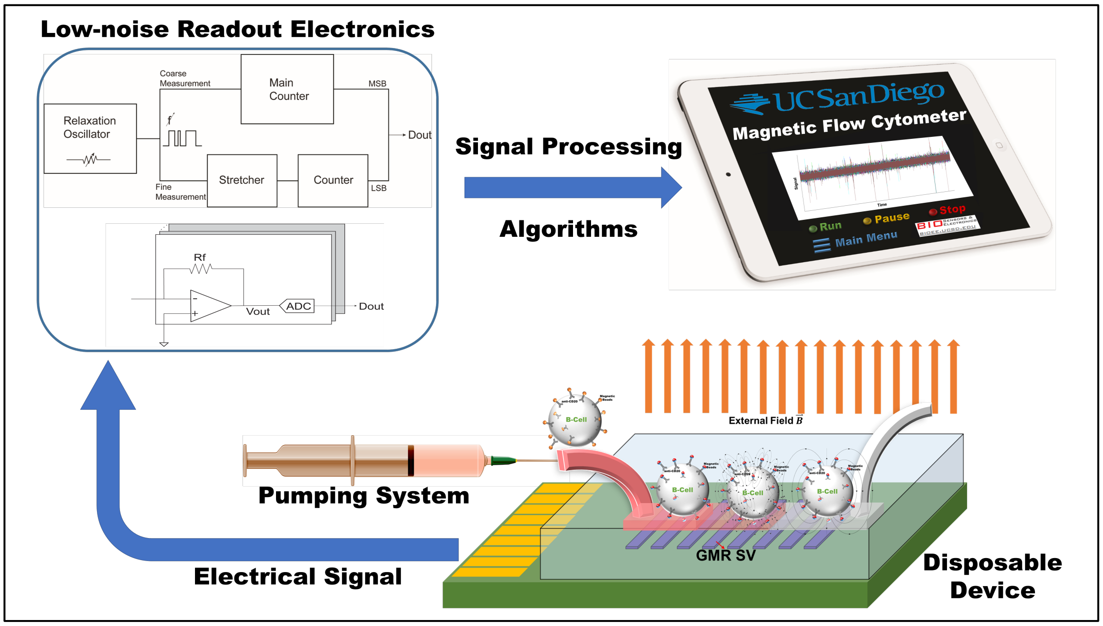

Figure 6.2: Point-of- care diagnostic device for clinical applications

REFERENCES

[1-1] *Economic Impact of Cancer*. Retrieved from http://www.cancer.org/cancer/cancerbasics/economic-impact-of-cancer.

[1-2] *Trends in Use and Expenditures for Cancer Treatment among Adults 18 and Older, U.S. Civilian Noninstitutionalized Population, 2001 and 2011*. Retrieved from http://meps.ahrq.gov/mepsweb/data_files/publications/st443/stat443.shtml.

[1-3] *Early detection of cancer*. Retrieved from http://www.who.int/cancer/detection/en/

[1-4] Giloh, H., & Sedat, J. W. (1982). Fluorescence microscopy: reduced photobleaching of rhodamine and fluorescein protein conjugates by n-propyl gallate. Science, 217(4566), 1252-1255

[1-5] Aubin, J. E. (1979). Autofluorescence of viable cultured mammalian cells. Journal of Histochemistry & Cytochemistry, 27(1), 36-43.

[1-6] Li, B., Zhang, X., & Zheng, J. (2015). Single-Cell Next-Generation Sequencing and Its Applications in Cancer Biology. In Next Generation Sequencing in Cancer Research, Volume 2 (pp. 1-18). Springer International Publishing.

[1-7] Brazaca, L., Ribovski, L., Janegitz, B., & Zucolotto, V. (2017). Nanostructured materials and nanoparticles for point of care (POC) medical biosensors. *Medical Biosensors for Point of Care (POC) Applications,* 229-254. doi:10.1016/b978-0-08-100072-4.00010-1

[2-1] Alivisatos, P. (2004). The use of nanocrystals in biological detection. Nature biotechnology, 22(1), 47-52.

[2-2] Yoffe, A. D. (2001). Semiconductor quantum dots and related systems: electronic, optical, luminescence and related properties of low dimensional systems. Advances in Physics, 50(1), 1-208.

[2-3] *Flow Cytometry - A Survey and the Basics*. Retrieved from http://www.labome.com/method/Flow-Cytometry-A-Survey-and-the-Basics.html.

[2-4] Xu, L., & Chen, H. (2014). Conformal transformation optics. *Nature Photonics,9*(1), 15-23. doi:10.1038/nphoton.2014.307

[2-5] Chatellus, H. G., Cortés, L. R., & Azaña, J. (2015). Optical real-time Fourier transformation with kilohertz resolutions. *Optica, 3*(1), 1. doi:10.1364/optica.3.000001

[2-6] Tsai, W., & Lin, Y. (2014). High-Throughput Optical Biosensing Arrays Detection Using White Light Fourier Transform Method. *Cleo: 2014*. doi:10.1364/cleo_at.2014.jth2a.93

[2-7] Ibrahim, S. F., & van den Engh, G. (2003). High-speed cell sorting: fundamentals and recent advances. Current opinion in biotechnology, 14(1), 5-12.

[2-8] Tzur, A., Moore, J. K., Jorgensen, P., Shapiro, H. M., & Kirschner, M. W. (2011). Optimizing optical flow cytometry for cell volume-based sorting and analysis. PloS one, 6(1), e16053.

[2-9] Willasch, A., Eing, S., Weber, G., Kuci, S., Schneider, G., Soerensen, J., ... & Bader, P. (2010). Enrichment of cell subpopulations applying automated MACS technique: purity, recovery and applicability for PCR-based chimerism analysis.Bone marrow transplantation, 45(1), 181-189.

[2-10] Zhu, H., & Ozcan, A. (2015). Opto-Fluidics Based Microscopy and Flow Cytometry on a Cell Phone for Blood Analysis. Mobile Health Technologies: Methods and Protocols, 171-190.

[2-11] Schena, M., Microarray Biochip Technology, 298, Eaton Publishing, Natick, 2000

[2-12] Lee, L. G., Nordman, E. S., Johnson, M. D., & Oldham, M. F. (2013). A low-cost, high-performance system for fluorescence lateral flow assays. Biosensors, 3(4), 360-373.

[2-13] Hong, B., Sun, A., Pang, L., Venkatesh, A. G., Hall, D., & Fainman, Y. (2015). Integration of Faradaic electrochemical impedance spectroscopy into a scalable surface plasmon biosensor for in tandem detection. Optics Express, 23(23), 30237-30249.

[2-14] Feng, L., Sivanesan, A., Lyu, Z., Offenhäusser, A., & Mayer, D. (2015). Electrochemical current rectification–a novel signal amplification strategy for highly sensitive and selective aptamer-based biosensor. Biosensors and bioelectronics, 66, 62-68.

[2-15] Akbari, E., Buntat, Z., Afroozeh, A., Zeinalinezhad, A., & Nikoukar, A. (2015). Escherichia coli bacteria detection by using graphene-based biosensor. Nanobiotechnology, IET, 9(5), 273-279.

[2-16] Shin, D. M., Shin, Y. C., Lee, J. H., Kim, T. H., Han, D. W., Kim, J. M., ... & Hwang, Y. H. (2015). Highly sensitive detection of epidermal growth factor

receptor expression levels using a capacitance sensor. Sensors and Actuators B: Chemical, 209, 438-443.

[2-17] Wilson, M. S. (2005). Electrochemical Immunosensors for the Simultaneous Detection of Two Tumor Markers. *Analytical Chemistry, 77*(5), 1496-1502. doi:10.1021/ac0485278

[2-18] D'orazio, P. (2003). Biosensors in clinical chemistry. *Clinica Chimica Acta, 334*(1-2), 41-69. doi:10.1016/s0009-8981(03)00241-9

[2-19] Abiri, H., Abdolahad, M., Gharooni, M., Hosseini, S. A., Janmaleki, M., Azimi, S., ... & Mohajerzadeh, S. (2015). Monitoring the spreading stage of lung cells by silicon nanowire electrical cell impedance sensor for cancer detection purposes. Biosensors and Bioelectronics, 68, 577-585.

[2-20] Chen, J., Xue, C., Zhao, Y., Chen, D., Wu, M. H., & Wang, J. (2015). Microfluidic Impedance Flow Cytometry Enabling High-Throughput Single-Cell Electrical Property Characterization. International journal of molecular sciences, 16(5), 9804-9830.

[2-21] Gawad, S., Schild, L., & Renaud, P. (2001). Micromachined impedance spectroscopy flow cytometer for cell analysis and particle sizing. Lab on a Chip, 1(1), 76-82.

[2-22] Eberbeck, D., Wiekhorst, F., Wagner, S., & Trahms, L. (2011). How the size distribution of magnetic nanoparticles determines their magnetic particle imaging performance. *Applied Physics Letters, 98*(18), 182502. doi:10.1063/1.3586776

[2-23] Guanxiong Li, "Spin valve sensor for biomolecular identification: design, fabrication and characterization," Ph.D. Thesis, Stanford University, 2005.

[2-24] Chemla, Y. R., Grossman, H. L., Poon, Y., McDermott, R., Stevens, R., Alper, M. D., & Clarke, J. (2000). Ultrasensitive magnetic biosensor for homogeneous immunoassay. Proceedings of the National Academy of Sciences, 97(26), 14268-14272

[2-25] Kleiner, R., Koelle, D., Ludwig, F., & Clarke, J. (2004). Superconducting quantum interference devices: State of the art and applications. Proceedings of the IEEE, 92(10), 1534-1548

[2-26] *Anisotropic magnetoresistance*. Retrieved from https://en.wikipedia.org/wiki/Magnetoresistance#Anisotropic_magnetoresistance_.28AMR.29

[2-27] Barnas, J., Fuss, A., Camley, R., Grünberg, P. & Zinn, W. Novel magnetoresistance effect in layered magnetic structures: Theory and experiment. Physical Review. B, Condensed Matter 42, 8110–8120 (1990).

[2-28] Li, G., Joshi, V., White, R. L., Wang, S. X., Kemp, J. T., Webb, C., . . . Sun, S. (2003). Detection of single micron-sized magnetic bead and magnetic nanoparticles using spin valve sensors for biological applications. Journal of Applied Physics, 93(10), 7557. doi:10.1063/1.1540176.

[2-29] Graham, D.L., Ferreira, H., Bernardo, J., Freitas, P.P. & Cabral, J.M.S. Single magnetic microsphere placement and detection on-chip using current line designs with integrated spin valve sensors: Biotechnological applications. 91, 7786–7788 (2002).

[2-30] Drew A. Hall, "GMR spin-valve biochips and interface electronics for ultrasensitive in-vitro diagnostics," Ph.D. Thesis, Stanford University, 2011.

[2-31] Fernandes, E., Martins, V., Nóbrega, C., Carvalho, C., Cardoso, F., Cardoso, S.Azeredo, J. (2014). A bacteriophage detection tool for viability assessment of Salmonella cells. *Biosensors and Bioelectronics, 52*, 239-246. doi:10.1016/j.bios.2013.08.053

[2-32] Shoshi, A., Schotter, J., Schroeder, P., Milnera, M., Ertl, P., Charwat, V., . . . Brueckl, H. (2012). Magnetoresistive-based real-time cell phagocytosis monitoring. *Biosensors and Bioelectronics, 36*(1), 116-122. doi:10.1016/j.bios.2012.04.002

[2-33] Lian, J., Chen, S., Qiu, Y., Zhang, S., Shi, S., & Gao, Y. (2012). A fully automated in vitro diagnostic system based on magnetic tunnel junction arrays and superparamagnetic particles. *Journal of Applied Physics, 111*(7). doi:10.1063/1.3675205

[2-34] Gaster, R. S., Xu, L., Han, S., Wilson, R. J., Hall, D. A., Osterfeld, S. J., . . . Wang, S. X. (2011). Quantification of protein interactions and solution transport using high-density GMR sensor arrays. *Nature Nanotechnology, 6*(5), 314-320. doi:10.1038/nnano.2011.45

[2-35] Martins, V., Cardoso, F., Germano, J., Cardoso, S., Sousa, L., Piedade, M., . . . Fonseca, L. (2009). Femtomolar limit of detection with a magnetoresistive biochip. *Biosensors and Bioelectronics, 24*(8), 2690-2695. doi:10.1016/j.bios.2009.01.040

[2-36] Shen, W., Schrag, B. D., Carter, M. J. & Xiao, G. Quantitative detection of DNA labeled with magnetic nanoparticles using arrays of MgO-based magnetic tunnel junction sensors. Applied Physics Letters 93, 3, doi:10.1063/1.2963970 (2008).

[2-37] Tondra, M., Porter, M. & Lipert, R. J. Model for detection of immobilized superparamagnetic nanosphere assay labels using giant magnetoresistive sensors.

Journal of Vacuum Science & Technology a-Vacuum Surfaces and Films 18, 1125-1129, doi:10.1116/1.582476 (2000).

[2-38] Baselt, D. R., Lee, G. U., Natesan, M., Metzger, S. W., Sheehan, P. E., & Colton, R. J. (1998). A biosensor based on magnetoresistance technology1This paper was awarded the Biosensors & Bioelectronics Award for the most original contribution to the Congress.1. *Biosensors and Bioelectronics, 13*(7-8), 731-739. doi:10.1016/s0956-5663(98)00037-2

[2-39] Schotter, J., Kamp, P., Becker, A., Pühler, A., Reiss, G., & Brückl, H. (2004). Comparison of a prototype magnetoresistive biosensor to standard fluorescent DNA detection. *Biosensors and Bioelectronics, 19*(10), 1149-1156. doi:10.1016/j.bios.2003.11.007

[2-40] Shen, W. F., Liu, X. Y., Mazumdar, D. & Xiao, G. In situ detection of single micron-sized magnetic beads using magnetic tunnel junction sensors. Applied Physics Letters 86, 3, doi:10.1063/1.1952582 (2005).

[2-41] Hall, D., Gaster, R., Lin, T., Osterfeld, S., Han, S., Murmann, B., & Wang, S. (2010). GMR biosensor arrays: A system perspective. *Biosensors and Bioelectronics,25*(9), 2051-2057. doi:10.1016/j.bios.2010.01.038

[3-1] Kim, D., Lee, J.-R., Shen, E., & Wang, S. X. (2013). Modeling and experiments of magneto-nanosensors for diagnostics of radiation exposure and cancer.*Biomedical Microdevices*, *15*(4), 665–671. http://doi.org/10.1007/s10544-012-9678-z

[3-2] Osterfeld SJ, Yu H, Gaster RS, Caramuta S, Xu L, Han S, Hall DA, Wilson RJ, Sun S, White RL, Davis RW, Pourmand N, Wang SX. Multiplex protein assays based on real-time magnetic nanotag sensing. Proceedings of the National Academy of Sciences. 2008;105:20637–20640.

[3-3] Fullerton, E. (2013, Spring Quarter) MATS251b. Lecture conducted from University of California, San Diego, CA.

[3-4] Ennen, I., Kappe, D., Rempel, T., Glenske, C., & Hütten, A. (2016). Giant Magnetoresistance: Basic Concepts, Microstructure, Magnetic Interactions and Applications. *Sensors (Basel, Switzerland)*, *16*(6), 904. http://doi.org/10.3390/s16060904

[3-5] Tokel, O., Yildiz, U. H., Inci, F., Durmus, N. G., & Sridhar, K. (2013). Portable Microfluidic integrated Plasmonic platform for Pathogen detection. Scientific Reports, 5, 9152. doi:10.1038/srep09152.

[3-6] Qin, D., Xia, Y., & Whitesides, G. M. (2010). Soft lithography for micro- and nanoscale patterning.*Nature Protocols*, *5*(3), 491–502. doi:10.1038/nprot.2009.234

[4-1] Lai, J. J., Nelson, K. E., Nash, M. A., Hoffman, A. S., Yager, P., & Stayton, P. S. (2009). Dynamic bioprocessing and microfluidic transport control with smart magnetic nanoparticles in laminar-flow devices. Lab on a Chip, 9(14), 1997.

[4-2] Fuerstman, M. J., Lai, A., Thurlow, M. E., Shevkoplyas, S. S., Stone, H. A., & Whitesides, G. M. (2007). The pressure drop along rectangular microchannels containing bubbles. Lab on a Chip, 7(11), 1479. doi:10.1039/b706549c

[4-3] Drew A.Hall, “GMR spin-valve biochips and interface electronics for ultrasensitive in-vitro diagnostics,” Ph.D. thesis, Stanford University, 2011

[5-1] Gao, Y., van Reenen, A., Hulsen, M. A., de Jong, A. M., Prins, M. W. J., & den Toonder, J. M. J. (2013). Disaggregation of microparticle clusters by induced magnetic dipole–dipole repulsion near a surface. Lab on a Chip, 13(7), 1394.

[6-1] Electric/Magnetic A New Perspective on Magnetic Field Sensing. Retrieved from http://www.sensorsmag.com/sensors/electric-magnetic/a-new-perspective-magnetic-field-sensing-855

[6-2] Qian, Z., Wang, D., Daughton, J., Tondra, M., Nordman, C., & Popple, A. (2004). Linear Spin-Valve Bridge Sensing Devices. IEEE Transactions on Magnetics, 40(4), 2643-2645.

[6-3] Eberbeck, D., Wiekhorst, F., Steinhoff, U., & Trahms, L. (2006). Aggregation behaviour of magnetic nanoparticle suspensions investigated by magnetorelaxometry. Journal of Physics: Condensed Matter, 18(38).

[6-4] Sin, M. L., Mach, K. E., Wong, P. K., & Liao, J. C. (2014). Advances and challenges in biosensor-based diagnosis of infectious diseases. Expert Review of Molecular Diagnostics, 14(2), 225-244.

[6-5] Klein, C. A. (2008). CANCER: The Metastasis Cascade. Science, 321(5897), 1785-1787.